Research Square

Preprints are preliminary reports that have not undergone peer review.
They should not be considered conclusive, used to inform clinical practice,
or referenced by the media as validated information.

Certified Error-Cancellation Scales for Gauss–Legendre Quadrature under Endpoint Double Scaling

Ming-Hung Shu

National Kaohsiung University of Science and Technology https://orcid.org/0000-0001-5866-6700

You-Pei Li

i1121431030@nkust.edu.tw

National Kaohsiung University of Science and Technology - Jiangong Campus: National Kaohsiung University of Science and Technology https://orcid.org/0000-0002-5323-2548

Research Article

Keywords: Gauss-Legendre quadrature, nearly singular integrals, hard-edge asymptotics, double-scaling limit, quadrature error, error cancellation

Posted Date: November 9th, 2026

DOI: https://doi.org/10.21203/rs.3.rs-11641326/v1

License: This work is licensed under a Creative Commons Attribution 4.0 International License.
Read Full License

Additional Declarations: The authors declare no competing interests.

Certified Error-Cancellation Scales for Gauss–Legendre Quadrature under Endpoint Double Scaling

Ming-Hung Shu, You-Pei Li *

Department of Industrial Engineering and Management, National Kaohsiung University of Science and Technology, Kaohsiung 807618, Taiwan

* **Correspondence:** Email: i112143103@nkust.edu.tw.

Abstract: Fixed-integrand quadrature error bounds do not describe what happens when a parameter-dependent endpoint singularity approaches the integration interval as the Gauss–Legendre order increases. We study the ordinary, unmodified rule for nearly singular kernels on $[0,2]$, under the coupled scaling $\delta \asymp N^{-4}$, where $N = n + 1/2$. Under explicit joint C^1 regularity and positivity conditions, the signed quadrature error has a locally uniform limit determined by endpoint data and a convergent Bessel-zero series. Analytic tail bounds and outward-rounded interval enclosures establish precisely one simple limiting zero in each of two disjoint parameter intervals. With additional C^3 regularity of the coefficients frozen at the singular parameter, we derive a next-order N^{-2} correction comprising a canonical contribution and two endpoint-slope terms. A lacunary Legendre-polynomial construction shows that joint C^1 regularity alone does not guarantee this correction. The next-order formula determines the displacement of any selected sequence of exact finite-order error-cancellation roots near either limiting zero, without assuming uniqueness at finite quadrature order. For a conservative bipolar electrostatic oscillator, the endpoint-slope terms vanish, leading to an explicit N^{-6} correction to its cancellation amplitude. Independent numerical checks of several kernel families and the oscillator complement the analytic results. The conclusions characterize signed-error transitions and isolated cancellation scales for the classical quadrature rule, rather than proposing an alternative integration scheme.

Keywords: Gauss-Legendre quadrature; nearly singular integrals; hard-edge asymptotics; double-scaling limit; quadrature error; error cancellation

1. Introduction

Gaussian quadrature converges rapidly for an integrand analytic in a fixed complex neighborhood of the integration interval. A different question arises when the integrand itself depends on a parameter and its nearest singularity approaches an endpoint as the quadrature order increases. Accuracy measured at a fixed parameter need not predict the error along such a coupled limit. We study this issue for the unmodified Gauss–Legendre rule applied to parameter-dependent nearly singular integrals.

The distinction between a fixed integrand and a parameter-dependent one matters especially at a critical endpoint. Let n denote the number of Gauss–Legendre nodes and let $\delta > 0$ measure the distance from the limiting singular parameter. In the model considered below, the smallest shifted Gauss–Legendre nodes are of order n^{-2}, while the endpoint regularization competes with their

squared distances. The resulting transition occurs at δ of order n^{-4}. Neither the fixed-n singular limit nor the large-n limit at fixed δ alone describes the signed quadrature error on this scale.

Lubinsky and Rabinowitz[1] examined convergence for Gaussian quadrature with singular integrands. Sidi[2] developed asymptotic Gauss–Legendre error expansions for fixed, integrable algebraic–logarithmic endpoint singularities. Its Theorem 2.1 gives an expansion uniform in the exponent on vertical strips, and Section 4 allows finite interior smoothness. A Mellin–Barnes representation of the canonical regularized kernel suggests a possible route from these fixed-integrand results, provided the inversion contour and remainder can be controlled uniformly in the coupled limit. Here we establish that limit directly for parameter-dependent continuously differentiable kernels and derive interval-certified sign changes and finite-order cancellation consequences. Generalized Gaussian rules and rational quadrature[3, 4] address different approximation strategies; classical special-function asymptotics and Gaussian-weight inequalities are used as established tools[5, 6].

Elliott et al.[7] investigated Gauss–Legendre quadrature errors for nearly singular boundary-element integrals, including inverse-square-root kernels. The present analysis instead addresses a singularity approaching an endpoint of the integration interval under coupled regularization–order scaling, establishing a locally uniform signed-error limit.

A more recent methodological comparison is given by Mitchell et al. [8], who study decomposition and conformal transformations to accelerate nearly singular quadrature when the nearby singularity is known. Their objective is to *improve* the computation through transformed integrands. By contrast, we characterize the signed error of the unmodified Gauss–Legendre rule under a simultaneous order–regularization limit.

As a physical example we use the conservative, symmetric bipolar electrostatic oscillator. Its reduced-order model appears in the MEMS vibration literature[9–15]; related investigations also address dynamic pull-in and periodic solutions in singular electrostatic models[16–18]. The free-oscillation period becomes logarithmically divergent as the turning point approaches a hyperbolic equilibrium. This separatrix behavior is classical[19, 20]. We derive the oscillator's parameter-explicit critical coefficient and constant as a baseline for the quadrature-error analysis. Low-order fixed-interval Gauss–Legendre approximations of nonlinear oscillator periods have been considered by Wu et al.[21] and Zhu et al.[22], providing an additional numerical motivation for assessing what changes close to a critical amplitude.

We establish a locally uniform coupled-limit theorem for parameter-dependent integrands of the form $f_\delta(x) = h(\delta, x)/\sqrt{m(\delta) + x^2 b(\delta, x)}$ on the shifted interval $[0,2]$. Under stated C^1 regularity and positivity hypotheses, we establish convergence of the signed quadrature error along $\delta = s(n + 1/2)^{-4}$. The normalized limit is an explicitly convergent series over positive zeros of J_0. Its coefficient and scaling argument are determined by endpoint data, despite changes in the remainder of the kernel with the regularization parameter. The theorem treats the coupled variation without assuming analyticity of the general kernel.

The limiting profile also yields error-cancellation results, which we interpret for a bipolar electrostatic oscillator. When the oscillator distance from critical amplitude is $s(n+1/2)^{-p}$, the ordinary Gauss–Legendre rule has three distinct error regimes: absolute-error convergence for $0 < p < 4$ (using the additional analyticity of this oscillator), a generally nonzero finite absolute-error limit for $p = 4$, and a nonvanishing limiting relative error for $p > 4$. Bessel-series tail bounds and certified interval enclosures establish a simple limiting root in each of two disjoint parameter intervals. Local uniform convergence and continuity imply an exact finite-order zero of the signed error in each interval for all sufficiently large orders.

Numerical calculations examine the joint-limit mechanism. Figures 1–4 and Tables 1–2 check the oscillator-period and fixed-order baselines. Numerical experiments with three distinct parameter-dependent families test the critical n^{-4} transition; Figure 5 displays the signed limiting error, and Figure 6 with Table 3 compares finite-order cancellation branches for a reference integral and the oscillator. Together they show why accuracy measured at a fixed subcritical parameter cannot be extrapolated blindly into the coupled limit and why cancellation at one parameter is not a neighborhood-wide accuracy guarantee.

Sections 2 and 3 derive the exact oscillator period and its critical asymptotics. Section 4 develops the quadrature results, including the coupled limit and cancellation scales, and Section 5 presents numerical tests. Section 6 concludes. Appendix A gives the analytical tail bounds and interval-enclosure procedure; Appendix B records the numerical methods and provenance of the results.

The analysis also resolves the first asymptotic correction beyond the limiting profile. Under a sufficient frozen-coefficient C^3 condition, the correction separates the canonical Legendre-ratio contribution from two terms determined by the spatial endpoint slopes of the numerator and denominator. The distinction is mathematically substantive: an explicit joint C^1 counterexample shows why the leading-order assumptions do not by themselves determine the next-order error. The correction additionally provides an asymptotic displacement formula for exact finite-order cancellation roots in the certified intervals; no finite-order uniqueness assumption is required.

For the electrostatic oscillator, the relevant frozen coefficients are even at the endpoint. Their first spatial derivatives therefore vanish, leaving only the canonical next-order correction and an explicit amplitude correction of order N^{-6}. Section 4.6 establishes these results, and Appendix C records the complex-uniform remainder argument and the Legendre-polynomial moment calculation used in the counterexample.

2. Governing model and exact period representation

2.1. Bipolar electrostatic oscillator

We consider the dimensionless single-degree-of-freedom model of a bipolar (double-sided) electrostatically actuated microbeam. This lumped representation has been widely used to describe the nonlinear free vibration and stability of double-sided electrostatic microstructures[10, 11, 15]. The governing equation is

$$\frac{d^2u}{dt^2} + g(u) = 0, \qquad g(u) = u - \beta\left[\frac{1}{(1-u)^2} - \frac{1}{(1+u)^2}\right], \qquad -1 < u < 1, \tag{2.1}$$

where u denotes the displacement normalized by the electrode gap and $\beta > 0$ is the dimensionless electrostatic parameter. The singular boundaries $u = \pm 1$ correspond to contact with the two electrodes. Because the configuration is symmetric, $g(u)$ is odd. We rewrite Eq (2.1) as

$$g(u) = u\left[1 - \frac{4\beta}{(1-u^2)^2}\right]. \tag{2.2}$$

The corresponding potential $U(u)$, normalized by $U(0) = 0$, is

$$U(u) = \frac{u^2}{2} - \frac{2\beta u^2}{1-u^2}, \qquad U'(u) = g(u). \tag{2.3}$$

We restrict the analysis to

$$0 < \beta < \frac{1}{4},$$

for which the origin is locally stable because $g'(0) = 1 - 4\beta > 0$. As will be established in Section 3, the system then possesses two symmetric nonzero unstable equilibria at $u = \pm A^\star(\beta)$, where the critical amplitude $A^\star(\beta)$ is determined by the equilibrium condition in Eq. (3.1).

For a free oscillation of amplitude $0 < A < A^\star$, we take $u(0) = A$ and $du/dt(0) = 0$. Conservation of mechanical energy gives

$$\frac{1}{2}\left(\frac{du}{dt}\right)^2 + U(u) = U(A). \tag{2.4}$$

Since the orbit is symmetric about $u = 0$, one quarter of the period corresponds to the motion from $u = A$ to $u = 0$. The exact period is therefore

$$T_e(A) = 4\int_0^A \frac{du}{\sqrt{2[U(A)-U(u)]}}. \tag{2.5}$$

For the potential in Eq (2.3), direct algebraic simplification gives the exact identity

$$2[U(A) - U(u)] = (A^2 - u^2)\left[1 - \frac{4\beta}{(1-A^2)(1-u^2)}\right]. \tag{2.6}$$

Equation (2.6) separates the ordinary turning-point factor $A^2 - u^2$ from the electrostatic factor that becomes critical as A approaches $A^\star$. We will use this factorization repeatedly in the asymptotic analysis of Section 3.

2.2. Fixed-interval representation

We first remove the regular turning-point factor in Eq (2.6) by introducing the trigonometric transformation $u = A\cos\tau$, where $0 \le \tau \le \pi/2$. For convenience, we define

$$\phi(A,\tau) = 1 - \frac{4\beta}{(1-A^2)(1-A^2\cos^2\tau)}. \tag{2.7}$$

Substituting Eq (2.6) and the transformation $u = A\cos\tau$ into Eq (2.5), the factor $A\sin\tau$ cancels exactly, and the exact period reduces to

$$T_e(A) = 4\int_0^{\pi/2} \frac{d\tau}{\sqrt{\phi(A,\tau)}}. \tag{2.8}$$

For every subcritical amplitude $0 < A < A^\star$, the integrand in Eq (2.8) is regular. In particular, $\phi(A,0) = 1 - 4\beta/(1-A^2)^2 > 0$, and $\phi(A,\tau)$ is monotonically increasing with τ on [0, π/2]. Hence $\phi(A,\tau)$ remains strictly positive throughout the integration interval for every $A < A^\star$. At the critical amplitude $A = A^\star$, however, this regularity is lost precisely at the endpoint $\tau = 0$. Section 3 will show that the resulting endpoint singularity is responsible for the logarithmic divergence of the exact period.

To place Eq (2.8) on the standard Gauss-Legendre interval, we introduce

$$\tau(t) = \frac{\pi(1+t)}{4}, \qquad f_A(t) = \frac{1}{\sqrt{\phi\left(A,\tau(t)\right)}}, \qquad -1 \le t \le 1. \tag{2.9}$$

Equation (2.8) then becomes

$$T_e(A) = \pi\int_{-1}^{1} f_A(t)\, dt. \tag{2.10}$$

The fixed-interval representation in Eqs (2.9) and (2.10) is the form used in the explicit quadrature framework developed by Wu et al.[21] and subsequently applied to large-amplitude string oscillations by Zhu et al.[22]. In the present problem, however, the parameter-dependent integrand $f_A(t)$ develops a qualitatively different endpoint structure as $A \to A^{\star-}$.

Let $t_i \in (-1,1)$, $i = 1, \ldots, n$, be a fixed finite set of interior quadrature nodes and let w_i denote the corresponding finite weights. We assume throughout that both the nodes and weights are independent of A. The associated period approximation is written as

$$T_n(A) = \pi\sum_{i=1}^{n} w_i f_A(t_i). \tag{2.11}$$

Equation (2.11) provides the general fixed-node form required for the analysis in Section 4. No positivity assumption on the weights is needed for the finite-ceiling result derived there.

For comparison with earlier low-order explicit approximations, we retain three representative quadrature formulas. The midpoint rule applied to Eq (2.10) gives

$$T_{\mathrm{MR}}(A) = 2\pi f_A(0). \tag{2.12}$$

The two-node Gauss-Legendre rule gives

$$T_{\mathrm{GL},2}(A) = \pi\left[f_A\left(-\frac{1}{\sqrt{3}}\right) + f_A\left(\frac{1}{\sqrt{3}}\right)\right]. \tag{2.13}$$

Similarly, the three-node Gauss-Legendre rule yields

$$T_{\mathrm{GL},3}(A) = \pi\left[\frac{5}{9}f_A\left(-\sqrt{\frac{3}{5}}\right) + \frac{8}{9}f_A(0) + \frac{5}{9}f_A\left(\sqrt{\frac{3}{5}}\right)\right]. \tag{2.14}$$

We use Eqs (2.12)–(2.14) only as explicit low-order benchmarks in the numerical comparisons. Our analytical conclusions are not restricted to these particular formulas. In Section 4, we first analyze the general fixed finite-node rule in Eq (2.11), and then specialize the result to the entire Gauss-Legendre family as the quadrature order n increases.

3. Critical saddle structure and logarithmic period asymptotics

3.1. Critical amplitude and local saddle structure

We first identify the phase-plane structure responsible for the singular growth of the period. For a nonzero equilibrium, Eq (2.2) requires the electrostatic factor in square brackets to vanish. Under the parameter restriction $0 < \beta < 1/4$, the physically admissible positive equilibrium therefore satisfies

$$[1-(A^\star)^2]^2 = 4\beta, \qquad A^\star(\beta) = \sqrt{1-2\sqrt{\beta}}, \qquad 1-(A^\star)^2 = 2\sqrt{\beta}. \quad (3.1)$$

The negative equilibrium is obtained by symmetry. Differentiating the restoring function in Eq (2.2) gives

$$g'(u) = 1 - \frac{4\beta(1+3u^2)}{(1-u^2)^3}, \qquad g'(A^\star) = 4 - \frac{2}{\sqrt{\beta}} < 0. \quad (3.2)$$

Hence the equilibria $u = \pm A^\star$ are local maxima of the potential and correspond to hyperbolic saddles of the first-order phase-plane system. We define the positive saddle rate by

$$\kappa(\beta) = \sqrt{-g'(A^\star)} = \sqrt{\frac{2}{\sqrt{\beta}} - 4} = \frac{2A^\star}{\sqrt{1-(A^\star)^2}}. \quad (3.3)$$

Because $U'(A^\star) = 0$ and $U''(A^\star) = g'(A^\star) = -\kappa^2$, the potential has the local expansion

$$U(u) = U(A^\star) - \frac{\kappa^2}{2}(A^\star - u)^2 + O((A^\star - u)^3), \qquad u \to A^{\star -}. \quad (3.4)$$

The same saddle structure is visible directly in the fixed-interval representation. Substituting Eq (3.1) into Eq (2.7) at the critical amplitude yields

$$\phi(A^\star, \tau) = \frac{(A^\star)^2 \sin^2\tau}{1-(A^\star)^2+(A^\star)^2\sin^2\tau}. \quad (3.5)$$

Consequently, as $\tau \to 0^+$,

$$\phi(A^\star, \tau) = \frac{(A^\star)^2}{1-(A^\star)^2}\tau^2 + O(\tau^4), \qquad \frac{1}{\sqrt{\phi(A^\star,\tau)}} = \frac{2}{\kappa\tau} + O(\tau). \quad (3.6)$$

Thus the critical integrand develops a nonintegrable $1/\tau$ endpoint singularity. Equation (3.6) identifies the local mechanism of the logarithmic divergence, but it does not by itself determine the logarithmic coefficient with respect to the physical distance $A^\star - A$ or the finite additive constant. These quantities require a near-critical analysis in which A approaches $A^\star$ simultaneously with the endpoint variable.

3.2. Two-term critical-period asymptotics

For the asymptotic analysis, let

$$a = A^{\star}, \qquad q = 1 - A^2, \qquad q_{\star} = 1 - a^2 = 2\sqrt{\beta}, \qquad \mu(A) = q - \frac{q_{\star}^2}{q}. \tag{3.7}$$

For $0 < A < a$, we have $q > q_{\star}$ and therefore $\mu(A) > 0$. Using $4\beta = q_{\star}^2$ in Eq (2.7), we obtain the exact factorization

$$\phi(A,\tau) = \frac{\mu(A)+A^2\sin^2\tau}{q+A^2\sin^2\tau}, T_e(A) = 4\int_0^{\pi/2} \frac{\sqrt{q+A^2\sin^2\tau}}{\sqrt{\mu(A)+A^2\sin^2\tau}} d\tau. \tag{3.8}$$

Theorem 3.1 (Two-term critical-period asymptotics)**.** *For every fixed* $0 < \beta < 1/4$*, the exact period in Eq (2.8) satisfies*

$$T_e(A) = -\frac{4}{\kappa(\beta)} \ln[A^*(\beta) - A] + C(\beta) + o(1), \qquad A \to A^{*-}, \tag{3.9}$$

where

$$C(\beta) = 4\arcsin A^* + \frac{4}{\kappa(\beta)} \ln\left(8A^*\sqrt{\beta}\right). \tag{3.10}$$

Proof.

We separate the regular and singular contributions in Eq (3.8) by writing

$$\frac{T_e(A)}{4} = R(A) + J(A), \tag{3.11}$$

where

$$R(A) = \int_0^{\pi/2} \frac{\sqrt{q+A^2\sin^2\tau}-\sqrt{q_{\star}}}{\sqrt{\mu(A)+A^2\sin^2\tau}} d\tau, J(A) = \sqrt{q_{\star}}\int_0^{\pi/2} \frac{d\tau}{\sqrt{\mu(A)+A^2\sin^2\tau}}. \tag{3.12}$$

The integrand defining $R(A)$ is regular in the joint limit $(A,\tau) \to (a,0)$. Indeed, after rationalizing its numerator and using $\mu(A) = (q - q_{\star})(q + q_{\star})/q$, the apparent endpoint singularity is removable and the integrand extends continuously to zero at $(a,0)$. Hence dominated convergence applies, and

$$\lim_{A\to a^-} R(A) = R_{\star} = a\int_0^1 \frac{dx}{\sqrt{1-a^2x^2}+\sqrt{q_{\star}}} = \arcsin a + \frac{\sqrt{q_{\star}}}{a} \ln \sqrt{q_{\star}}. \tag{3.13}$$

The singular term can be written in terms of the complete elliptic integral of the first kind K. Specifically,

$$J(A) = \frac{\sqrt{q_{\star}}}{\sqrt{A^2+\mu(A)}} K\left(\frac{A}{\sqrt{A^2+\mu(A)}}\right). \tag{3.14}$$

As its modulus approaches unity, Section 19.12 of the NIST Handbook of Mathematical Functions[5] gives

$$K(k) = \ln\left(\frac{4}{\sqrt{1-k^2}}\right) + o(1), \qquad k \to 1^-. \tag{3.15}$$

Meanwhile, the parameter $\mu(A)$ satisfies

$$\mu(A) = \frac{(q-q_{\star})(q+q_{\star})}{q}, \qquad \lim_{A\to a^-} \frac{\mu(A)}{a-A} = 4a. \tag{3.16}$$

Substituting Eqs (3.15) and (3.16) into Eq (3.14) therefore yields

$$J(A) = -\frac{\sqrt{q_{\star}}}{2a} \ln(a - A) + \frac{\sqrt{q_{\star}}}{2a} \ln(4a) + o(1). \tag{3.17}$$

Combining Eqs (3.11), (3.13), and (3.17), and using $\kappa = 2a/\sqrt{q_\star}$ and $q_\star = 2\sqrt{\beta}$, gives Eq (3.9) with the constant in Eq (3.10).

□

The logarithmic coefficient $4/\kappa$ is determined entirely by the local saddle curvature, whereas the additive constant $C(\beta)$ contains both the local critical scale and the regular contribution of the remaining orbit. For the present bipolar electrostatic oscillator, Eq (3.10) therefore provides a fully parameter-explicit two-term critical-period law rather than only the leading logarithmic divergence. The closed-form expression will be verified independently against numerical evaluation of the exact period in Section 5.

4. Structural limitation and endpoint double-scaling error

4.1. Finite critical ceiling

We now consider the critical behavior of the general fixed finite-node approximation in Eq (2.11). For later comparison, we define the relative error by

$$E_n(A) = \frac{T_n(A) - T_e(A)}{T_e(A)}. \tag{4.1}$$

Theorem 4.1 (Finite critical ceiling of fixed interior-node rules)**.** *Let $t_i \in (-1,1)$, $i = 1, \dots, n$, be a fixed finite set of interior nodes and let w_i be finite weights. Suppose that both the nodes and weights are independent of A. Then, for every fixed $\beta \in (0,1/4)$,*

$$\lim_{A \to A^{\star -}} T_n(A) = T_n(A^\star) = \pi \sum_{i=1}^{n} w_i \, f_{A^\star}(t_i) < \infty. \tag{4.2}$$

Consequently,

$$\lim_{A \to A^{\star -}} \frac{T_n(A)}{T_e(A)} = 0, \qquad \lim_{A \to A^{\star -}} E_n(A) = -1. \tag{4.3}$$

Proof. For every interior node $t_i > -1$, the corresponding angle $\tau_i = \pi(1 + t_i)/4$ satisfies $\tau_i > 0$. Equation (3.5) therefore gives $\phi(A^\star, \tau_i) > 0$. Since $\phi(A, \tau_i)$ depends continuously on A, each $f_A(t_i) = \phi(A, \tau_i)^{-1/2}$ has a finite limit as $A \to A^{\star -}$. The finite sum in Eq (2.11) consequently converges to Eq (4.2). By Theorem 3.1, however, $T_e(A) \to \infty$ logarithmically. Dividing the finite limit in Eq (4.2) by the divergent exact period gives the first limit in Eq (4.3), and the second follows from Eq (4.1). □

Theorem 4.1 does not require positive weights and is therefore not tied to a particular classical quadrature family. Its essential hypotheses are only that the number of nodes is finite, that every node remains strictly inside the interval, and that the nodes and weights are fixed before the critical-amplitude limit is taken.

4.2. Gauss-Legendre critical-ceiling asymptotics

We next determine how the finite ceiling changes when the order of Gauss-Legendre quadrature is increased. Set

$$q_\star = 1 - a^2 = 2\sqrt{\beta}, \qquad a = A^\star. \tag{4.4}$$

At the critical amplitude, Eqs (2.7), (2.9), and (3.5) give

$$f_\star(t) := f_{A^\star}(t) = \frac{\sqrt{q_\star + a^2 \sin^2\left(\frac{\pi(1+t)}{4}\right)}}{a \sin\left(\frac{\pi(1+t)}{4}\right)}. \tag{4.5}$$

Using $\kappa = 2a/\sqrt{q_\star}$, the endpoint expansion of Eq (4.5) can be written in the form

$$f_\star(t) = \frac{8}{\pi\kappa}\frac{1}{1+t} + r(t), \qquad -1 < t \le 1, \tag{4.6}$$

where r extends continuously to $[-1,1]$ and $r(-1) = 0$.

Lemma 4.2 (Gauss-Legendre harmonic-number identity)**.** *Let* $t_i^{(n)}$ *and* $w_i^{(n)}$, $i = 1, \dots, n$, *be the nodes and weights of the* n*-point Gauss-Legendre rule on* $[-1,1]$. *Then*

$$\sum_{i=1}^{n} \frac{w_i^{(n)}}{1+t_i^{(n)}} = 2H_n, \qquad H_n = \sum_{k=1}^{n} \frac{1}{k}. \tag{4.7}$$

Proof. Let P_n denote the Legendre polynomial normalized by $P_n(1) = 1$ and define

$$p_{n-1}(t) = \frac{1-(-1)^n P_n(t)}{1+t}. \tag{4.8}$$

Because $P_n(-1) = (-1)^n$, the apparent pole at $t = -1$ is removable and p_{n-1} is a polynomial of degree $n-1$. At every Gauss-Legendre node, $P_n\left(t_i^{(n)}\right) = 0$, so $p_{n-1}\left(t_i^{(n)}\right) = \left(1 + t_i^{(n)}\right)^{-1}$. Exactness of the n-point rule for polynomials of degree at most $2n-1$ therefore yields

$$\sum_{i=1}^{n} \frac{w_i^{(n)}}{1+t_i^{(n)}} = \int_{-1}^{1} p_{n-1}(t)\, dt = \int_{-1}^{1} \frac{1-P_n(x)}{1-x}\, dx. \tag{4.9}$$

The telescoping identity $1 - P_n = \sum_{k=1}^{n}(P_{k-1} - P_k)$, together with

$$\frac{P_{k-1}(x) - P_k(x)}{1-x} = \frac{1}{k}\frac{d}{dx}[P_{k-1}(x) + P_k(x)], \tag{4.10}$$

gives $\int_{-1}^{1}(P_{k-1} - P_k)/(1-x)\, dx = 2/k$. Summation over k proves Eq (4.7). □

Theorem 4.3 (Gauss-Legendre growth for a simple endpoint pole)**.** *Let* $c \in \mathbb{R}$ *and* $r \in C[-1,1]$, *and define* $F(t) = c/(1+t) + r(t)$ *for* $-1 < t \le 1$. *Let* $Q_n[F] = \sum_{i=1}^{n} w_i^{(n)} F\left(t_i^{(n)}\right)$ *denote the* n*-point Gauss-Legendre sum. Then*

$$Q_n[F] = 2c \ln n + C_F + o(1), \qquad C_F = 2c\gamma + \int_{-1}^{1} r(t)\, dt.$$

When the pole coefficient is nonzero, the function is nonintegrable at the left endpoint; nevertheless, the discrete sum is well defined for every order because all Gauss-Legendre nodes lie strictly inside the interval. Thus the theorem characterizes the asymptotic growth of the discrete sums and does not assign a finite value to the divergent integral.

Proof. By Lemma 4.2, $Q_n[F] = 2cH_n + Q_n[r]$. It remains to show $Q_n[r] \to \int_{-1}^{1} r\,(t)\,dt$. Given $\varepsilon > 0$, the Weierstrass approximation theorem gives a polynomial p satisfying $\| r - p \|_\infty < \varepsilon$. For all sufficiently large n, Gauss-Legendre exactness gives $Q_n[p] = \int_{-1}^{1} p\,(t)\,dt$. Since the Gauss-Legendre weights are positive and sum to 2,

$$\left| Q_n[r] - \int_{-1}^{1} r\,(t)\,dt \right| \le 4 \| r - p \|_\infty < 4\varepsilon.$$

Hence $Q_n[r] \to \int_{-1}^{1} r\,(t)\,dt$. Together with $H_n = \ln n + \gamma + o(1)$, the stated expansion follows. □

Corollary 4.4 (Large-order critical ceiling)**.** *For fixed $\beta \in (0,1/4)$, the n-point Gauss-Legendre critical ceiling satisfies*

$$T_{\mathrm{GL},n}(A^\star) = \frac{16}{\kappa}\ln n + D(\beta) + o(1), \qquad n \to \infty, \tag{4.11}$$

where

$$D(\beta) = 4\arcsin a + \frac{16\gamma}{\kappa} + \frac{8}{\kappa}\ln\left(\frac{4\sqrt{q_\star}}{\pi}\right), \tag{4.12}$$

and γ denotes the Euler-Mascheroni constant.

Proof. Equation (4.6) has the form required by Theorem 4.3 with $c = 8/(\pi\kappa)$. After restoring the prefactor π in Eq (2.10), Theorem 4.3 gives the logarithmic coefficient $16/\kappa$ in Eq (4.11). The calculation below evaluates the finite constant $D(\beta)$ explicitly.

Applying the Gauss-Legendre rule to the decomposition in Eq (4.6) and using Lemma 4.2 gives

$$T_{\mathrm{GL},n}(A^\star) = \frac{16}{\kappa} H_n + \pi \sum_{i=1}^{n} w_i^{(n)}\, r\left(t_i^{(n)}\right). \tag{4.13}$$

Because r is continuous on $[-1,1]$, Gauss-Legendre quadrature converges for the second term[6]. Hence

$$\pi \sum_{i=1}^{n} w_i^{(n)}\, r\left(t_i^{(n)}\right) \to \pi \int_{-1}^{1} r\,(t)\,dt. \tag{4.14}$$

The remaining integral is evaluated directly from Eq (4.5). With $\tau = \pi(1+t)/4$,

$$\pi \int_{-1}^{1} r\,(t)\,dt = 4 \lim_{\varepsilon \to 0^+} \left[\int_{\varepsilon}^{\pi/2} \frac{\sqrt{q_\star + a^2 \sin^2\tau}}{a \sin\tau}\, d\tau - \frac{2}{\kappa}\ln\left(\frac{\pi}{2\varepsilon}\right) \right]. \tag{4.15}$$

If $\theta_\varepsilon = \arcsin(a\cos\varepsilon)$, elementary substitutions give

$$\int_{\varepsilon}^{\pi/2} \frac{\sqrt{q_\star + a^2 \sin^2\tau}}{a \sin\tau}\, d\tau = \theta_\varepsilon + \frac{2}{\kappa}\operatorname{artanh}\left(\frac{\sqrt{q_\star}}{a}\tan\theta_\varepsilon\right). \tag{4.16}$$

Since $\theta_\varepsilon \to \arcsin a$ and

$$\operatorname{artanh}\left(\frac{\sqrt{q_\star}}{a}\tan\theta_\varepsilon\right) = \ln\left(\frac{2\sqrt{q_\star}}{\varepsilon}\right) + o(1), \tag{4.17}$$

Eqs (4.15)-(4.17) yield

$$\pi \int_{-1}^{1} r\,(t)\,dt = 4\arcsin a + \frac{8}{\kappa}\ln\left(\frac{4\sqrt{q_\star}}{\pi}\right). \tag{4.18}$$

Finally, $H_n = \ln n + \gamma + o(1)$. Substitution of Eq (4.18) into Eqs (4.13) and (4.14) gives Eqs (4.11) and (4.12). □

4.3. Pointwise versus nonuniform convergence

For every fixed subcritical amplitude $A < A^\star$, the function f_A is analytic on the closed integration interval. The standard convergence of Gauss-Legendre quadrature[6] therefore gives

$$\lim_{n\to\infty} T_{\mathrm{GL},n}(A) = T_e(A), \qquad 0 < A < A^\star. \tag{4.19}$$

This pointwise convergence does not extend uniformly in relative error to the complete subcritical interval. Indeed, Theorem 4.1 gives, for every finite n,

$$\lim_{A\to A^{\star-}} E_{\mathrm{GL},n}(A) = -1. \tag{4.20}$$

Thus, for every finite n, the supremum of $\left|E_{\mathrm{GL},n}(A)\right|$ over $0 < A < A^*$ is at least 1; it therefore cannot tend to zero as $n \to \infty$. Increasing the quadrature order shifts the onset of the critical discrepancy closer to $A^\star$, but no fixed finite order removes it.

Remark 4.5 (Endpoint inclusion)**.** The interior-node assumption in Theorem 4.1 identifies one structural mechanism, but simply adding the singular endpoint does not recover the correct critical law. At $t = -1$,

$$f_A(-1) = \frac{1}{\sqrt{\phi(A,0)}} \sim \sqrt{\frac{q_\star}{4a}}\,(a - A)^{-1/2}, \qquad A \to a^-. \tag{4.21}$$

Therefore, a fixed quadrature rule carrying a nonzero weight at $t = -1$ would introduce an algebraic divergence proportional to $(a - A)^{-1/2}$ rather than the logarithmic divergence in Theorem 3.1. Resolving the critical limit requires a quadrature or analytical treatment adapted to the shrinking endpoint layer, rather than the mere inclusion of a fixed endpoint sample.

4.4. Critical double-scaling quadrature error

The fixed-order ceiling established above does not describe a simultaneous approach to the critical endpoint and to increasing quadrature order. To quantify this transition, consider the shifted Gauss–Legendre integral family

$$I(\delta) = \int_0^2 f_\delta\,(x)\,dx, \qquad f_\delta(x) = \frac{h(\delta,x)}{\sqrt{m(\delta)+x^2 b(\delta,x)}}. \tag{4.22}$$

Assume $h, b \in C^1([0,\delta_0]\times[0,2])$ with $b(\delta,x) \geq b_* > 0$. Assume also $m \in C([0,\delta_0])$, $m(0) = 0$, $m(\delta) > 0$ for all sufficiently small $\delta > 0$, and $m(\delta) = m_1\delta + O(\delta^2)$ as $\delta \downarrow 0$, where $m_1 > 0$. Put $h_0 = h(0,0) \neq 0$, $b_0 = b(0,0) > 0$, and $c = h_0/\sqrt{b_0}$. The continuity of m is retained explicitly because the later finite-order cancellation argument uses continuity of the signed error as a function of the regularization parameter. Here Q_n denotes the ordinary n-point Gauss–Legendre rule on $[0,2]$, with positive weights and interior nodes.

Let j_k denote the kth positive zero of J_0, define $v_k = j_k^2/2$, and introduce

$$L(\lambda) = 2\sum_{k=1}^{\infty} \frac{1}{J_1(j_k)^2}\left(\frac{1}{v_k} - \frac{1}{\sqrt{v_k^2+\lambda}}\right), \qquad G(\lambda) = 2\gamma - \log 4 + \frac{1}{2}\log\lambda - L(\lambda). \tag{4.23}$$

Theorem 4.6 (critical double-scaling limit)**.** *For fixed $s > 0$, put $N = n + \frac{1}{2}$, $\delta_n = sN^{-4}$ and $\lambda = m_1 s/b_0$. Then*

$$Q_n(0) - Q_n(\delta_n) \to cL(\lambda), \qquad Q_n(\delta_n) - I(\delta_n) \to cG(\lambda). \tag{4.24}$$

These limits are locally uniform in $s > 0$, and the first limit is uniform for bounded nonnegative s. In particular, the limiting signed absolute error depends on the endpoint data through only c and λ; the global shape of h and b does not enter the leading profile.

Proof. Let the increasing nodes on $[0,2]$ be $x_{k,n}$ with corresponding weights $w_{k,n}$. The classical Mehler–Heine endpoint limit and the Gauss-weight formula[5, 6] give, for each fixed $k \geq 1$,

$$N^2 x_{k,n} \to v_k, \qquad N^2 w_{k,n} \to \frac{2}{J_1(j_k)^2}.$$

Since $m(\delta) = m_1\delta + O(\delta^2)$ and h, b are C^1, rationalization of the denominator gives the uniform bound

$$|f_0(x) - f_\delta(x)| \leq C\delta x^{-3}, \qquad 0 < x \leq 2.$$

Standard Legendre zero-angle estimates and the Chebyshev–Markov–Stieltjes inequalities for the Gauss weights imply that the first half of the nodes obey $x_{k,n} \geq C_1 k^2 N^{-2}$ and $w_{k,n} \leq C_2 k N^{-2}$. The remaining nodes stay uniformly away from the left endpoint. Consequently, for $\delta = sN^{-4}$ and $K \leq \lfloor n/2 \rfloor$,

$$\sum_{k>K} w_{k,n}\left|f_0(x_{k,n}) - f_{sN^{-4}}(x_{k,n})\right| \leq CsK^{-4} + CsN^{-4}.$$

At each fixed endpoint index, the weighted difference tends to

$$\frac{2c}{J_1(j_k)^2}\left(\frac{1}{v_k} - \frac{1}{\sqrt{v_k^2+\lambda}}\right).$$

The uniform tail estimate justifies passage from the fixed-index limits to the entire Gauss sum. Thus $Q_n(0) - Q_n(sN^{-4}) \to cL(\lambda)$, uniformly for s on bounded nonnegative intervals.

For the signed-error limit, write $f_0(x) = c/x + g(x)$, where the C^1 hypotheses ensure that g extends continuously to the left endpoint. The exact Gauss–Legendre identity $Q_n(1/x) = 2H_n$ and convergence for continuous g yield

$$Q_n(0) = 2c\log N + 2c\gamma + \int_0^2 g\,(x)\,dx + o(1).$$

Writing $\rho = m_1\delta/b_0$, subtraction of the canonical singular kernel $c/\sqrt{x^2+\rho}$ leaves a uniformly bounded remainder converging pointwise to g.

To establish domination, set $B_\delta(x) = m(\delta) + x^2 b(\delta, x)$ and $B_\delta^0(x) = m_1\delta + b_0 x^2$. Uniform positivity and the first-order endpoint expansions give, for sufficiently small positive δ,

$$B_\delta(x) \asymp B_\delta^0(x) \asymp x^2 + \delta, \qquad \left|B_\delta(x) - B_\delta^0(x)\right| \le C\{\delta^2 + x^2(x+\delta)\}.$$

Also, $|h(\delta, x) - h_0| \le C(x+\delta)$. Subtracting the canonical term and rationalizing the denominators therefore bounds the remainder in absolute value by

$$C\frac{x+\delta}{\sqrt{x^2+\delta}} + C\frac{\delta^2 + x^2(x+\delta)}{(x^2+\delta)^{3/2}} \le C', \qquad 0 \le x \le 2.$$

The bound is independent of the regularization parameter and supplies an integrable majorant on the fixed interval. At each positive interior point, the remainder tends to the continuous function already identified in the proof. This supplies the claimed convergence of its integral without requiring analyticity or higher differentiability of the general kernel. Dominated convergence now yields the integral expansion below.

$$I(\delta) = c\operatorname{arsinh}\left(\frac{2}{\sqrt{\rho}}\right) + \int_0^2 g\,(x)\,dx + o(1) = c(\log 4 - 1/2\log\rho) + \int_0^2 g\,(x)\,dx + o(1).$$

For $\delta = sN^{-4}$, one has $\rho = \lambda N^{-4}$. Combining this integral expansion with the quadrature expansion and the first limit proves $Q_n(sN^{-4}) - I(sN^{-4}) \to cG(\lambda)$. The same estimates imply locally uniform convergence for $s > 0$. ▫

To apply the general theorem to the physical period, let $\delta = a - A$ and set $x = 1 + t$, so that $\tau = \pi x/4$. The *complete period*, including the factor π in Eq. (2.10), then has the form in Eq. (4.22), with

$$h(\delta, x) = \pi\sqrt{q + A^2\sin^2(\pi x/4)}, \qquad m(\delta) = \mu(A), \qquad b(\delta, x) = A^2\left[\frac{\sin(\pi x/4)}{x}\right]^2, \qquad A = a - \delta.$$

At $x = 0$ the quotient in b is defined by its removable limit $\pi/4$. Since $a > 0$ for each fixed $0 < \beta < 1/4$, these functions are C^1 on a sufficiently small closed parameter rectangle, b is bounded below by a positive constant, and $m(\delta) > 0$ for $\delta > 0$. Equations (3.7) and (3.16) give $m(\delta) = 4a\delta + O(\delta^2)$. Therefore

$$h_0 = \pi\sqrt{q_\star}, \qquad b_0 = \frac{a^2\pi^2}{16}, \qquad m_1 = 4a, \qquad \frac{h_0}{\sqrt{b_0}} = \frac{8}{\kappa}, \qquad \frac{m_1 s}{b_0} = \frac{64s}{a\pi^2}.$$

These bounds verify the hypotheses of Theorem 4.6 for the oscillator.

For the electrostatic oscillator of Section 2, the endpoint coefficients are

$$c = \frac{8}{\kappa}, \qquad \lambda = \frac{64s}{a\pi^2}, \qquad a = \sqrt{1 - 2\sqrt{\beta}}. \tag{4.25}$$

Hence the oscillator-specific limiting error is $\Psi_\beta(s) = (8/\kappa)G\big(64s/(a\pi^2)\big)$. This is the parameter-normalized crossover used in Section 5. The critical scaling concerns $\delta \asymp N^{-4}$, rather than a universal loss of accuracy for every subcritical amplitude.

4.5. Path-dependent error regimes and cancellation scales

Corollary 4.7 (three approach regimes for the bipolar oscillator)**.** *Fix* $0 < \beta < 1/4$*, let* $a = A^*(\beta)$ *and* $N = n + 1/2$*, and define* $A_n = a - sN^{-p}$ *for fixed* $s > 0$ *and* $p > 0$*. Let* $T_{\mathrm{GL},n}(A_n)$ *be ordinary* n*-point Gauss–Legendre quadrature of the exact period integral. Then the following statements hold:*

1. *If* $0 < p < 4$*, the absolute error* $T_{\mathrm{GL},n}(A_n) - T_e(A_n)$ *tends to zero.*
2. *If* $p = 4$*, the signed absolute error converges to* $(8/\kappa)G\big(64s/(a\pi^2)\big)$*, while the relative error tends to zero.*
3. *If* $p > 4$*, the relative error tends to* $4/p - 1$*, and the absolute error has the logarithmic behavior*

$$\frac{T_{\mathrm{GL},n}(A_n)}{T_e(A_n)} - 1 \to \frac{4}{p} - 1, \qquad T_{\mathrm{GL},n}(A_n) - T_e(A_n) = -\frac{4(p-4)}{\kappa}\log N + O(1).$$

Proof. The statements for $p = 4$ follow from Theorem 4.6 and the oscillator endpoint data in Eq. (4.25), together with $T_e(a - sN^{-4}) \sim (16/\kappa)\log N$. If $p > 4$, the difference estimate used in proving Theorem 4.6 gives $T_{\mathrm{GL},n}(a) - T_{\mathrm{GL},n}(a - sN^{-p}) = O(N^{4-p}) = o(1)$; here $T_{\mathrm{GL},n}(a)$ denotes the critical finite-node value. Corollary 4.4 yields $T_{\mathrm{GL},n}(a) = (16/\kappa)\log N + O(1)$, whereas Theorem 3.1 gives $T_e(a - sN^{-p}) = (4p/\kappa)\log N + O(1)$. Subtracting and dividing establish (3).

For (1), the oscillator kernel is analytic at each strictly subcritical amplitude. Its nearest moving complex denominator zeros have distance of order $\delta^{1/2}$ from the critical endpoint, where $\delta = a - A$. For sufficiently small fixed $\eta > 0$, choose a Bernstein ellipse of parameter $\rho_\delta = 1 + \eta\delta^{1/4}$ on which the integrand is holomorphic and has supremum bounded by $C\delta^{-1/2}$. The standard analytic Gauss–Legendre estimate applies with the factor $(\rho_\delta - 1)^{-1}$.

The ellipse choice is uniform for each fixed admissible electrostatic parameter: the numerator stays separated from zero in a sufficiently small complex neighborhood of the real interval, while the moving denominator zeros are the only singularities approaching the left endpoint. A sufficiently small ellipse-opening constant keeps those zeros outside the contour, and compactness controls the remaining part of the interval. Thus the stated supremum estimate and the exponential quadrature bound apply with constants independent of the approaching amplitude, although the constants may depend on the fixed electrostatic parameter.

To make the ellipse separation explicit, use the shifted interval $[0,2]$ and write $z = x + iy$ and $t = \rho_\delta - 1 = \eta\delta^{1/4}$. The corresponding shifted Bernstein ellipse has semiaxes $a_t = \big(\rho_\delta + \rho_\delta^{-1}\big)/2$

and $b_t = \left(\rho_\delta - \rho_\delta^{-1}\right)/2$. Its interior satisfies $-Ct^2 \le x \le 2 + Ct^2$ and $y^2 \le Ct^2(|x| + t^2) \le C\eta^2(x^2 + \delta)$ for sufficiently small δ, with constants independent of δ.

The identity $\mathrm{Re}\{\sin^2(\pi z/4)\} = \sin^2(\pi x/4) - \cos(\pi x/2)\sinh^2(\pi y/4)$, the endpoint expansion $m(a-\delta) = 4a\delta + O(\delta^2)$, and $\sin^2(\pi x/4) \ge cx^2$ on this real projection together imply $\mathrm{Re}\{m(a-\delta) + (a-\delta)^2\sin^2(\pi z/4)\} \ge c_\beta(\delta + x^2)$ when η is chosen sufficiently small. The square-root denominator consequently admits a holomorphic branch throughout the ellipse and its inverse is bounded there by $C\delta^{-1/2}$. The numerator is also holomorphic and uniformly bounded because its squared radicand stays away from zero near the real interval. The uniform ellipse bound therefore yields the analytic quadrature estimate for this oscillator, without any additional assumption on the general C^1 family.

$$\left|T_{\mathrm{GL},n}(a-\delta) - T_e(a-\delta)\right| \le C\delta^{-3/4}\exp\left(-c_0 n\delta^{1/4}\right), \qquad 0 < \delta < \delta_0.$$

When $\delta = sN^{-p}$ with $0 < p < 4$, the exponent grows in magnitude as $-cN^{1-p/4}$ and dominates the algebraic factor. Hence the absolute error vanishes. This part uses the oscillator's analyticity and is not a conclusion for arbitrary C^1 kernels in Theorem 4.6. ▫

We next make the error-cancellation statement precise. For $K \ge 1$, let $L_K(\lambda)$ be the first K terms of the Bessel series $L(\lambda)$ in Eq. (4.23). The bounds derived in Appendix A establish

$$0 < L(\lambda) - L_K(\lambda) < \frac{\lambda}{\pi^4(K - 1/4)^4}, \qquad \lambda > 0.$$

Using $K = 24$ and certified enclosures of the Bessel zeros and their values under J_1, the following strict sign intervals hold for the complete infinite-series function:

$$-0.00009720 < G(4.15) < -0.00009704, \qquad 0.00024104 < G(4.16) < 0.00024120,$$
$$0.00000880 < G(76.8) < 0.00001132, \qquad -0.00001581 < G(77) < -0.00001330.$$

The corresponding derivative enclosures are positive throughout $(4.15,4.16)$ and negative throughout $(76.8,77)$, as detailed in Appendix A. These signs establish one simple root in each of the two specified intervals; they do not establish a global root count. Approximate root values used in the plots are $\lambda_1 \approx 4.1528672585$ and $\lambda_2 \approx 76.87311692$.

Proposition 4.8 (finite-order exact cancellation in two prescribed brackets)**.** *Under the assumptions of Theorem 4.6, write* $B_1 = (4.15,4.16)$ *and* $B_2 = (76.8,77)$. *For each* $i \in \{1,2\}$ *and every sufficiently large* n, *there exists* $\lambda_{i,n} \in B_i$ *such that*

$$Q_n\left(\frac{b_0\lambda_{i,n}}{m_1N^4}\right) - I\left(\frac{b_0\lambda_{i,n}}{m_1N^4}\right) = 0, \qquad \lambda_{i,n} \to \lambda_i.$$

Here λ_i *is the unique root of* G *within* B_i. *Finite-*n *root uniqueness, and any explicit minimal quadrature order at which each branch exists, are not claimed.*

Proof. For each fixed sufficiently large n, the assumed continuity of m, h and b, together with positivity of the denominator for positive regularization, makes $Q_n(\delta) - I(\delta)$ continuous on a sufficiently small positive interval. Theorem 4.6 gives uniform convergence of this signed error to $cG(\lambda)$ when $\delta = b_0\lambda/(m_1N^4)$ and λ ranges over either closed bracket. Because $c \ne 0$ and G has opposite signs at the endpoints of each bracket, the finite-order error has opposite endpoint signs for all sufficiently large n. The intermediate value theorem therefore gives at least one zero in each

bracket. Any convergent subsequence of such zeros must limit to a zero of G in its bracket by uniform convergence; bracketwise uniqueness of λ_i implies convergence of the entire selected sequence. ▫

Figure 5 visualizes the profile, while Figure 6 and Table 3 illustrate the finite-order behavior and the importance of the sufficiently-large-n qualifier.

4.6. Next-order signed-error asymptotics and cancellation-root displacement

The leading-order result in Theorem 4.6 identifies the endpoint data that determine the signed Gauss–Legendre error under the scaling $\delta \asymp N^{-4}$. We next distinguish the universal correction of the canonical kernel from the first correction caused by the spatial variation of the coefficients. The regularity needed for this second-order statement is stronger than that required for Theorem 4.6.

Throughout this subsection, write

$$\mathcal{E}_n[u] := Q_n[u] - \int_0^2 u\,(x)\,dx, \qquad N = n + 1/2,$$

where $Q_n[u]$ is the ordinary n-point Gauss–Legendre rule on $[0,2]$. To avoid confusion with this quadrature notation, $\mathrm{Q}_n(z)$ will denote the Legendre function of the second kind, whereas $P_n(z)$ denotes the Legendre polynomial. For $\rho > 0$ set

$$K_\rho(x) = (x^2+\rho)^{-1/2}, \qquad q_\rho(x) = x(x^2+\rho)^{-1/2}, \qquad p_\rho(x) = x^3(x^2+\rho)^{-3/2}.$$

The functions G and $v_k = j_k^2/2$ retain the definitions in Section 4.4. Put $A_k = 2/J_1(j_k)^2$ and define, for $\lambda > 0$,

$$\begin{aligned} H_1(\lambda) &= \sqrt{\lambda} + \sum_{k=1}^{\infty} A_k \left(\frac{v_k}{\sqrt{v_k^2+\lambda}} - 1 \right), \\ H_3(\lambda) &= 2\sqrt{\lambda} + \sum_{k=1}^{\infty} A_k \left(\frac{v_k^3}{(v_k^2+\lambda)^{3/2}} - 1 \right), \\ \mathcal{K}(\lambda) &= \frac{H_3(\lambda) - 2H_1(\lambda) + \lambda G'(\lambda)}{6}. \end{aligned}$$

Both series converge absolutely and locally uniformly, and termwise differentiation shows

$$H_3(\lambda) = H_1(\lambda) + 2\lambda H_1{}'(\lambda).$$

Thus H_1 and H_3 are related profiles, not independent special functions.

Lemma 4.9 (canonical and basis-kernel corrections). *For every compact interval $J \subset (0,\infty)$, as $n \to \infty$, uniformly for $\lambda \in J$,*

$$\begin{aligned} \mathcal{E}_n[K_{\lambda N^{-4}}] &= G(\lambda) + N^{-2}\mathcal{K}(\lambda) + O_J(N^{-4}), \\ N^2\mathcal{E}_n[q_{\lambda N^{-4}}] &\to H_1(\lambda), \\ N^2\mathcal{E}_n[p_{\lambda N^{-4}}] &\to H_3(\lambda). \end{aligned}$$

Proof. For q_ρ, use $Q_n[1] = 2$ and the exact identity $\int_0^2 q_\rho \, dx = \sqrt{4+\rho} - \sqrt{\rho}$, obtaining

$$N^2 \mathcal{E}_n[q_{\lambda N^{-4}}] = \sum_{k=1}^{n} N^2 \, w_{k,n}\big(q_{\lambda N^{-4}}(x_{k,n}) - 1\big) + N^2 \left(2 - \sqrt{4 + \lambda N^{-4}} + \sqrt{\lambda} N^{-2}\right).$$

The last term tends to $\sqrt{\lambda}$. The fixed-index node and weight limits in Section 4.4 give the summands in the definition of H_1. For the first half of the nodes, the bound

$$0 \le 1 - q_\rho(x) \le \frac{\rho}{2x^2}, \qquad x_{k,n} \ge Ck^2 N^{-2}, \quad w_{k,n} \le CkN^{-2},$$

implies $N^2 w_{k,n} \left| q_\rho(x_{k,n}) - 1 \right| \le C_J k^{-3}$; the remaining nodes contribute $O_J(N^{-2})$. Finite-head convergence followed by a uniform summable-tail estimate proves the second assertion. The same argument applies to p_ρ, using

$$0 \le 1 - p_\rho(x) \le \frac{3\rho}{2x^2}, \qquad \int_0^2 p_\rho \, dx = \sqrt{4+\rho} + \frac{\rho}{\sqrt{4+\rho}} - 2\sqrt{\rho},$$

and yields the third assertion. Differentiating the H_1 series on compact positive λ-intervals proves $H_3 = H_1 + 2\lambda H_1'$.

For the canonical assertion, introduce the ratio

$$r_n(\zeta) = \frac{\mathrm{Q}_n(1 + \zeta N^{-2})}{P_n(1 + \zeta N^{-2})}, \qquad p_0(\zeta) = I_0\big(\sqrt{2\zeta}\big), \qquad r_0(\zeta) = \frac{K_0\big(\sqrt{2\zeta}\big)}{I_0\big(\sqrt{2\zeta}\big)},$$

with the branches obtained by continuation from $\mathrm{Re}\zeta > 0$. The exact Stieltjes-transform identity for Gauss–Legendre quadrature and the elementary Cauchy-kernel representation give

$$\mathcal{E}_n[K_{\lambda N^{-4}}] = -\frac{2}{\pi} \int_0^{\pi} r_n\left(i\sqrt{\lambda}\cos\theta\right) d\theta.$$

The Legendre polynomial has the exact finite series

$$P_n(1 + \zeta N^{-2}) = \sum_{k=0}^{n} \frac{(\zeta/2)^k}{(k!)^2} \prod_{j=0}^{k-1} \left(1 - \frac{(j+1/2)^2}{N^2}\right).$$

The factorial denominator gives a normally convergent majorant on every fixed complex compact set. Taylor expansion of the finite products gives a locally uniform expansion of the polynomial and, through the exact Wronskian relation,

$$r_n'(\zeta) = -\frac{1}{(2\zeta + \zeta^2 N^{-2}) P_n(1 + \zeta N^{-2})^2},$$

of the derivative of the ratio. The integration constant follows from the exact expansion at $\zeta = 0$:

$$\lim_{\zeta\to 0}(r_n(\zeta) + 1/2\log\zeta) = \log N + 1/2\log 2 - H_n.$$

Since $H_n = \log N + \gamma + (24N^2)^{-1} + O(N^{-4})$, the result is

$$r_n(\zeta) = r_0(\zeta) + \frac{2\zeta - 1}{24N^2 p_0(\zeta)^2} + O_K(N^{-4})$$

on fixed compact subsets of a slit neighborhood of the required imaginary segment. The difference $r_n - r_0$ has a removable singularity at $\zeta = 0$. The auxiliary difference whose quotient by ζ is used in the uniform bound has an exact zero there; the detailed complex-uniform remainder argument is given in Appendix C. The uniform expansion therefore extends across the point where the integration segment passes through zero. The function p_0 has no zeros on this segment, and hence the denominator stays bounded away from zero in a sufficiently small fixed neighborhood. Integrating the expansion gives

$$\mathcal{E}_n[K_{\lambda N^{-4}}] = G(\lambda) + \frac{1}{12\pi N^2}\int_0^{\pi} \frac{1 - 2i\sqrt{\lambda}\cos\theta}{I_0\left(\sqrt{2i\sqrt{\lambda}\cos\theta}\right)^2}\, d\theta + O_J(N^{-4}).$$

The leading integral agrees with G by Theorem 4.6. To identify the coefficient, put $\langle F\rangle_\lambda = \pi^{-1}\int_0^{\pi} F\left(i\sqrt{\lambda}\cos\theta\right) d\theta$. The exact Cauchy-kernel formulas yield $H_1 = 2\langle \zeta r_0\rangle_\lambda$ and $G = -2\langle r_0\rangle_\lambda$. Using $r_0' = -[2\zeta p_0^2]^{-1}$ and the identity for H_3, the displayed integral coefficient equals $[H_3 - 2H_1 + \lambda G']/6 = \mathcal{K}$. This completes the proof. ▫

Theorem 4.10 (next-order universality for parameter-dependent kernels). *Assume all hypotheses of Theorem 4.6 and, in addition,*

$$h(0,\cdot),\ b(0,\cdot) \in C^3[0,2].$$

Define $c = h_0/\sqrt{b_0}$, $\alpha = h_x(0,0)/\sqrt{b_0}$, $\beta_1 = b_x(0,0)/b_0$, *and* $\delta_n(\lambda) = b_0\lambda/(m_1 N^4)$. *Then, for every compact* $J \subset (0,\infty)$, *uniformly for* $\lambda \in J$,

$$\boxed{\mathcal{E}_n\left[f_{\delta_n(\lambda)}\right] = cG(\lambda) + \frac{c\mathcal{K}(\lambda) + \alpha H_1(\lambda) - \frac{1}{2}c\beta_1 H_3(\lambda)}{N^2} + o_J(N^{-2}).}$$

No joint C^3 *regularity in* (δ, x) *and no differentiability of* m *are assumed.*

Proof. Freeze the coefficients at $\delta = 0$:

$$\bar{f}_\delta(x) = \frac{h(0,x)}{\sqrt{m_1\delta + x^2 b(0,x)}}, \qquad \rho = \frac{m_1\delta}{b_0}.$$

Joint C^1 regularity, $m(\delta) = m_1\delta + O(\delta^2)$, and denominator positivity imply

$$\left|f_\delta(x) - \bar{f}_\delta(x)\right| \le \frac{C\delta}{\sqrt{x^2+\delta}}.$$

Using positivity of the rule, $Q_n[1/x] = 2H_n$, and $\int_0^2 (x^2+\delta)^{-1/2}\,dx = O(1+|\log\delta|)$, we find

$$\sup_{\lambda\in J}\left|\mathcal{E}_n\left[f_{\delta_n} - \bar{f}_{\delta_n}\right]\right| = O_J\left(N^{-4}(1+\log N)\right).$$

Set $H(x) = h(0,x)/\sqrt{b_0}$, $B(x) = b(0,x)/b_0$, and $\mathcal{A}(x,r) = H(x)/\sqrt{B(x)+r}$. The exact first-order Taylor formula in x, with r fixed, gives

$$\bar{f}_\delta = cK_\rho + \alpha q_\rho - \frac{c\beta_1}{2}p_\rho + R_\rho,$$

where

$$R_\rho(x) = xU(x,\rho/x^2), \qquad U(x,r) = \int_0^1 (1-t)\,\mathcal{A}_{xx}(tx,r)\,dt,$$

and $R_\rho(0) = 0$ is the removable value. Uniform boundedness of $\mathcal{A}_{xx}$ and $\partial_r\mathcal{A}_{xx}$ for $x \in [0,2]$ and $r \ge 0$ yields

$$\left|R_\rho(x) - R_0(x)\right| \le C\min\{x, \rho/x\}, \qquad x > 0.$$

Splitting the integral at $x = \sqrt{\rho}$ and invoking $Q_n[1/x] = 2H_n$ gives

$$\left|\mathcal{E}_n\left[R_\rho - R_0\right]\right| = O_J\left(N^{-4}(1+\log N)\right).$$

Writing $A_0(x) = H(x)/\sqrt{B(x)}$, one has

$$R_0(x) = \frac{A_0(x) - A_0(0)}{x} - A_0'(0) = \int_0^1 A_0\,'(tx)\,dt - A_0'(0).$$

The additional frozen C^3 assumption gives $R_0 \in C^2[0,2]$. Standard polynomial approximation implies $e_d(R_0) = o(d^{-2})$, where e_d is best uniform approximation by polynomials of degree at most d. The degree-$(2n-1)$ exactness of Gauss–Legendre quadrature and its positivity therefore imply

$$|\mathcal{E}_n[R_0]| \le 4e_{2n-1}(R_0) = o(N^{-2}).$$

Combining (A)–(C) with Lemma 4.9 proves the claimed locally uniform expansion. ▫

Remark (scope of the regularity condition). The frozen C^3 assumption is sufficient, not asserted to be sharp. The proof also works under frozen C^2 regularity together with the direct approximation condition $e_{2n-1}(R_0) = o(N^{-2})$. The counterexample below shows only that the original joint C^1 condition is insufficient for a universal next-order law determined solely by the endpoint slopes.

The exact Legendre moment and the lacunary-tail comparison used in the following example are detailed in Appendix C.

Example 4.11 (failure of the next-order law under joint C^1 alone). Let P_m denote the standard Legendre polynomial on $[-1,1]$, and put

$$m_j = 2^{2^j}, \qquad a_j = 2^{-j}, \qquad \Phi_m(t) = (1-t^2)^2 P_m(t)^2, \qquad g(x) = \sum_{j=1}^{\infty} a_j \, \Phi_{m_j}(x-1).$$

Classical Legendre bounds imply $\| \Phi_m \|_\infty \le C/m$ and $\| \Phi_m{}' \|_\infty \le C$, so the series for g and g' converge uniformly. Thus $g \in C^1[0,2]$, $g \ge 0$, $g(0) = g'(0) = 0$, and $g(x) \le Cx^2$. Choose

$$h(\delta, x) = 1 + xg(x), \qquad b(\delta, x) = 1, \qquad m(\delta) = \delta.$$

These functions satisfy every assumption of Theorem 4.6, with $c = 1$ and both endpoint slopes equal to zero. Nevertheless, for $n = m_j$, all terms of g with index $i < j$ are integrated exactly, while $Q_{m_j}\left[\Phi_{m_j}(\cdot - 1)\right] = 0$ because its values vanish at the Gaussian nodes. Moreover,

$$\int_{-1}^{1} \Phi_m(t)\, dt = \frac{3}{8m} + O(m^{-2}),$$

and the total contribution of indices $i > j$ is $o\left(a_j/m_j\right)$ by the lacunarity of m_j. Hence

$$\mathcal{E}_{m_j}[g] \sim -\frac{3a_j}{8m_j}, \qquad \left(m_j + 1/2\right)^2 \mathcal{E}_{m_j}[g] \to -\infty.$$

For $\rho = \lambda N^{-4}$, $f_\rho - K_\rho = g q_\rho$. Since $g(x) \le Cx^2$ and $0 \le 1 - q_\rho(x) \le \rho/(2x^2)$,

$$\left| \mathcal{E}_n[g q_\rho] - \mathcal{E}_n[g] \right| \le C\rho.$$

Thus the N^2-scaled kernel-dependent correction diverges along $n = m_j$, although both endpoint slopes vanish. Consequently the conclusion of Theorem 4.10 cannot be extended to all joint C^1 families without an additional global approximation requirement.

Corollary 4.12 (displacement of exact cancellation roots). *Suppose the hypotheses of Theorem 4.10 hold. Let* $B_1 = (4.15, 4.16)$, $B_2 = (76.8, 77)$, *and let* λ_i *be the unique simple zero of*

G in B_i, as certified in Appendix A. For each sufficiently large n, select any $\lambda_{i,n} \in B_i$ satisfying $\mathcal{E}_n\left[f_{\delta_n(\lambda_{i,n})}\right] = 0$. Then

$$\boxed{N^2(\lambda_{i,n} - \lambda_i) \to -\frac{c\mathcal{K}(\lambda_i) + \alpha H_1(\lambda_i) - \frac{1}{2}c\beta_1 H_3(\lambda_i)}{cG'(\lambda_i)}.}$$

Finite-n uniqueness of these roots is not asserted.

Proof. Proposition 4.8 gives the existence of zeros for sufficiently large n, and its compactness argument shows that every such selected sequence converges to λ_i. Let $F(\lambda) = c\mathcal{K}(\lambda) + \alpha H_1(\lambda) - \frac{1}{2}c\beta_1 H_3(\lambda)$. Theorem 4.10 gives

$$0 = cG(\lambda_{i,n}) + N^{-2}F(\lambda_{i,n}) + o(N^{-2}),$$

with a remainder uniform on the closure of B_i. Since $cG'(\lambda_i) \neq 0$, the mean-value theorem first gives $\lambda_{i,n} - \lambda_i = O(N^{-2})$. Taylor expansion of G at λ_i and continuity of F then yield the stated limit. This argument does not differentiate the finite-order error and therefore requires no derivative assumption on m. ▫

Corollary 4.13 (electrostatic-oscillator cancellation amplitude). *Fix an admissible oscillator parameter $0 < \beta < 1/4$, write $a = A^*(\beta)$, and adopt κ from Section 3. The oscillator coefficients in Section 4.4 satisfy*

$$c = \frac{8}{\kappa}, \qquad \lambda = \frac{64s}{a\pi^2}, \qquad h_x(0,0) = b_x(0,0) = 0.$$

Hence for every compact $J \subset (0,\infty)$,

$$\mathcal{E}_n[f_{\delta_n(\lambda)}] = \frac{8}{\kappa}\left(G(\lambda) + \frac{\mathcal{K}(\lambda)}{N^2}\right) + o_J(N^{-2}).$$

In particular, if $A_{i,n} = a - \delta_n(\lambda_{i,n})$ is any exact cancellation amplitude corresponding to the i-th certified bracket, then

$$\boxed{A_{i,n} = a - \frac{a\pi^2\lambda_i}{64N^4} + \frac{a\pi^2}{64N^6}\frac{\mathcal{K}(\lambda_i)}{G'(\lambda_i)} + o(N^{-6}).}$$

Proof. The oscillator expressions for h and b involve $\sin^2(\pi x/4)$ and $[\sin(\pi x/4)/x]^2$. Their frozen versions extend smoothly and are even in x near zero, so both endpoint derivatives vanish. Theorem 4.10 and Corollary 4.12 apply, while $\delta_n(\lambda) = a\pi^2\lambda/(64N^4)$ gives the final change of variables. ▫

5. Numerical verification and discussion

5.1. Verification of the critical-period asymptotics

Figures 1–4 and Tables 1–2 were produced using MATLAB[23]. Independent tests of the hard-edge limit across three integral families, and the finite-order cancellation calculations summarized in Sections 5.4–5.5 and Table 3, were conducted separately. The numerical comparisons use the recorded source data without interpolation or adjustment.

For Table 1, the numerical asymptotic constant is evaluated from three geometrically spaced near-critical distances using arbitrary-precision period integration followed by two Richardson elimination steps. The tabulated values use the three-distance extrapolation routine. Reported absolute differences are computed from the unrounded internal values, even where the two displayed columns coincide at twelve decimal places; these discrepancies are not interval bounds.

We first verify the analytical results of Section 3 using the representative parameter value $\beta = 0.05$. For this case, the closed-form expressions give $A^\star = 0.7434961$, $\kappa = 2.2235719$, and $C(\beta) = 3.866151384655$. We evaluate the exact period from Eq (2.8), using high-precision numerical integration in the near-critical regime, and compare it with both the three-node Gauss-Legendre approximation and the two-term asymptotic law in Theorem 3.1.

Figure 1 shows the exact period $T_e(A)$, the three-node approximation $T_{\mathrm{GL},3}(A)$, and the two-term asymptotic approximation as functions of the normalized amplitude $A/A^\star$. Over most of the subcritical interval, $T_{\mathrm{GL},3}(A)$ is visually indistinguishable from the exact period. Their limiting behavior is nevertheless fundamentally different. As $A \to A^{\star-}$, the exact period increases without bound, whereas the three-node approximation approaches the finite critical ceiling $T_{\mathrm{GL},3}(A^\star) = 15.965949$. The two-term asymptotic approximation, in contrast, follows the increasing exact period in the near-critical regime. Figure 1 therefore illustrates simultaneously the accuracy of the low-order quadrature formula away from the critical boundary and its structural inability to reproduce the critical divergence.

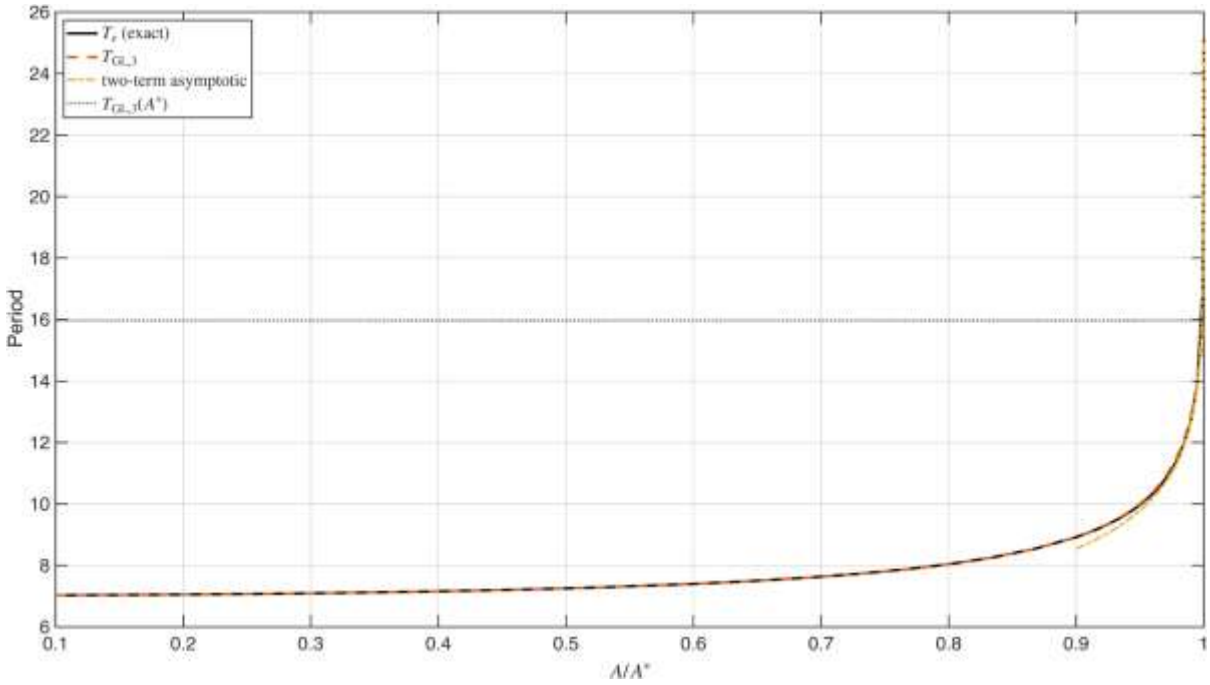


Figure 1. Exact period $T_e(A)$, three-node Gauss-Legendre approximation $T_{\mathrm{GL},3}(A)$, and the two-term critical-period asymptotic approximation for $\beta = 0.05$. The horizontal dotted line denotes the finite critical ceiling $T_{\mathrm{GL},3}(A^\star)$.

The corresponding phase-plane structure is shown in Figure 2. We compute the trajectories directly from the energy relation in Eq (2.4) for $A/A^\star = 0.30,\ 0.60,\ 0.85,\ 0.95$, and 0.99. As the amplitude increases, the periodic orbits expand toward the unstable equilibria $u = \pm A^\star$. The outer trajectories increasingly approach the saddle locations before returning, consistently with the local structure established in Section 3.1. This progressive saddle approach provides the phase-plane interpretation of the rapid period growth near the critical amplitude.

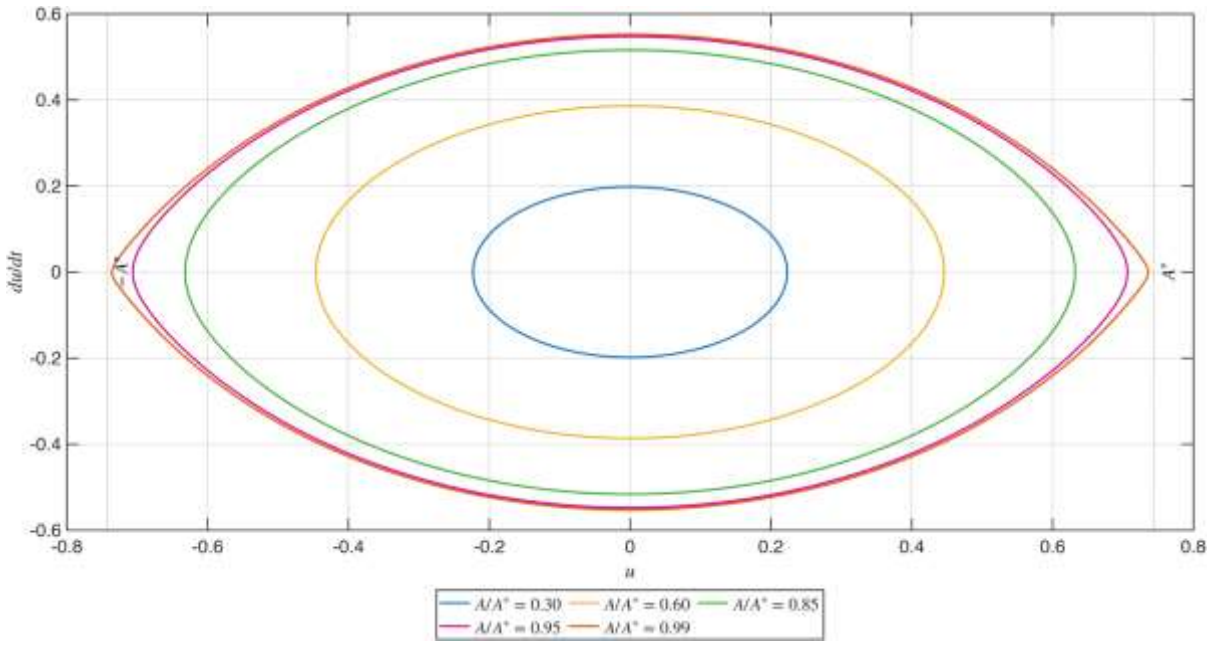


Figure 2. Phase trajectories for $\beta = 0.05$ at $A/A^\star = 0.30,\ 0.60,\ 0.85,\ 0.95,$ and 0.99. The dashed vertical lines indicate the unstable equilibria $u = \pm A^\star$.

To test not only the logarithmic coefficient but also the finite constant in Theorem 3.1, we evaluate the residual quantity

$$G(A) = T_e(A) + \frac{4}{\kappa}\ln(A^\star - A). \tag{5.1}$$

Figure 3 shows this quantity over several decades of $A^\star - A$. It converges to the analytical value $C(0.05) = 3.866151384655$, with the numerical curve becoming visually indistinguishable from the closed-form limit in the near-critical regime. The numerical values are consistent with the full two-term expansion, including its finite constant.

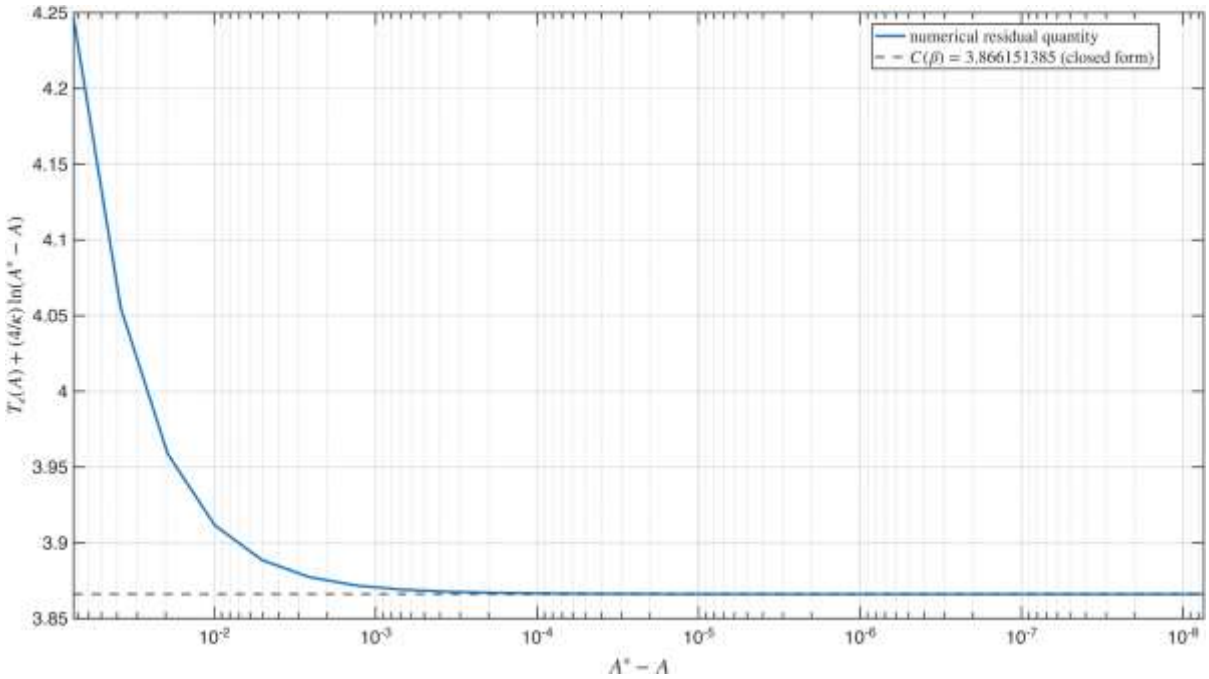


Figure 3. Numerical convergence of $T_e(A) + (4/\kappa)\ln(A^\star - A)$ toward the closed-form constant $C(\beta)$ for $\beta = 0.05$. The horizontal dashed line denotes $C(0.05) = 3.866151384655$.

The parameter-explicit critical-period constant in Eq. (3.10) is assessed at eight representative values of β. Table 1 compares the closed-form constants with independent numerical extrapolations of the residual in Eq. (5.1). The archived numerical implementation evaluates this residual at three relative critical distances 10^{-6}, 10^{-7} and 10^{-8} using 80-digit working precision. Writing the three residuals as R_1, R_2 and R_3, its two first-stage extrapolations are $R_{12} = (10R_2 - R_1)/9$ and $R_{23} = (10R_3 - R_2)/9$; the reported estimate is then $(100R_{23} - R_{12})/99$. Independent high-precision recomputation of these three-distance extrapolations agrees with the analytical constants to all 12 decimal places displayed. The last-column differences are floating-point numerical discrepancies, not

certified error bounds. The Table 1 estimates were generated by the three-distance extrapolation routine rather than the earlier single-distance implementation.

Table 1. Closed-form values of the asymptotic constant $C(\beta)$ and independent high-precision numerical extrapolations for representative values of β.

β	$A^\star$	κ	$C(\beta)$, *closed form*	$C(\beta)$, *numerical*	$\lvert\Delta C\rvert$
0.02	0.8468514	3.1846720	3.986389539890	3.986389539890	2.75×10^{-14}
0.05	0.7434961	2.2235719	3.866151384655	3.866151384655	1.60×10^{-14}
0.08	0.6590255	1.7524462	3.790149507794	3.790149507794	1.33×10^{-14}
0.10	0.6062545	1.5246492	3.727446402715	3.727446402715	1.20×10^{-14}
0.12	0.5542379	1.3317292	3.638784947871	3.638784947871	1.15×10^{-14}
0.15	0.4747666	1.0788780	3.409724808408	3.409724808408	1.02×10^{-14}
0.18	0.3891939	0.8450120	2.916708915912	2.916708915912	1.20×10^{-14}
0.20	0.3249197	0.6871215	2.200090086284	2.200090086284	1.29×10^{-14}

5.2. Fixed-order quadrature accuracy and critical breakdown

We next examine how the asymptotic limitation proved in Theorem 4.1 emerges from the finite-amplitude numerical results. Table 2 compares the exact period with the midpoint, two-node Gauss-Legendre, and three-node Gauss-Legendre approximations for $\beta = 0.05$. At small and moderate amplitudes, all three rules are accurate, with the three-node rule giving the smallest error over most of the regular regime. For example, the relative error of $T_{\mathrm{GL},3}$ is -0.006565% at $A/A^\star = 0.70$, 0.041162% at $A/A^\star = 0.90$, and 0.312266% at $A/A^\star = 0.95$.

The behavior changes rapidly once the amplitude enters the immediate neighborhood of $A^\star$. At $A/A^\star = 0.99$, the relative error of the three-node rule is 1.247991%. It subsequently changes sign and reaches -8.280103%, -24.130587%, and -36.439200% at $A/A^\star = 0.999$, 0.9999, and 0.99999, respectively. At the last of these amplitudes, the exact period is 25.110051, whereas the three-node rule gives only 15.960150, already close to its finite critical ceiling.

The same mechanism is visible more strongly for the lower-order rules. At $A/A^\star = 0.99999$, the midpoint and two-node Gauss-Legendre relative errors are -59.513658% and -46.009244%, respectively. These results are consistent with Eq (4.3): for every fixed finite rule, the exact period continues to diverge while the numerical approximation remains bounded, so the relative error ultimately approaches -1. The finite-amplitude calculations in Table 2 should therefore not be interpreted as a gradual loss of quadrature accuracy for a fixed regular integrand. They represent the onset of the singular limiting process described by Theorem 4.1.

Table 2. Exact period and fixed-order quadrature approximations for $\beta = 0.05$, together with their relative errors, from the regular regime to the immediate neighborhood of $A^\star$.

$A/A^\star$	T_e	T_{MR}	RE_{MR} (%)	T_{GL2}	RE_{GL2} (%)	T_{GL3}	RE_{GL3} (%)
0.100000	7.032159	7.032154	−0.000058	7.032160	0.000014	7.032158	−0.000001
0.300000	7.095795	7.095411	−0.005406	7.095887	0.001300	7.095786	−0.000121
0.500000	7.255973	7.251802	−0.057478	7.256970	0.013749	7.255884	−0.001227
0.700000	7.634483	7.604210	−0.396532	7.641533	0.092346	7.633982	−0.006565
0.900000	8.921867	8.603287	−3.570770	8.981690	0.670528	8.925539	0.041162
0.950000	9.973245	9.182157	−7.932104	10.070499	0.975149	10.004388	0.312266
0.990000	12.717161	9.917821	−22.012308	12.300711	−3.274714	12.875870	1.247991
0.999000	16.828908	10.139978	−39.746663	13.402578	−20.359787	15.435457	−8.280103
0.999900	20.968195	10.163748	−51.527790	13.542702	−35.413125	15.908447	−24.130587
0.999990	25.110051	10.166141	−59.513658	13.557107	−46.009244	15.960150	−36.439200

5.3. Large-order behavior of the Gauss-Legendre critical ceiling

Finally, we verify the large-order result in Corollary 4.4. For each Gauss-Legendre order n, we evaluate the quadrature rule directly at $A = A^\star$. Every finite-order value remains finite, as required by Theorem 4.1, but the sequence of critical ceilings increases systematically with n.

The upper panel of Figure 4 plots $T_{GL,n}(A^\star)$ against $\ln n$. The computed sequence approaches the analytical large-order law in Eq (4.11). For $\beta = 0.05$, Eq (4.12) gives $D(\beta) = 6.928052039048$. The lower panel removes the leading logarithmic term and plots $T_{GL,n}(A^\star) - (16/\kappa)\ln n$. The resulting sequence converges toward the predicted value of $D(\beta)$, consistent with both the logarithmic growth rate and the finite constant in Corollary 4.4.

As an additional numerical check on Lemma 4.2, we evaluated the identity in Eq (4.7) for $n = 2,4,\ldots,512$. Over this range, the absolute numerical discrepancy remained below 4.1×10^{-12}, consistent with floating-point accumulation in the computed Gauss-Legendre nodes and weights and with the exact analytical identity.

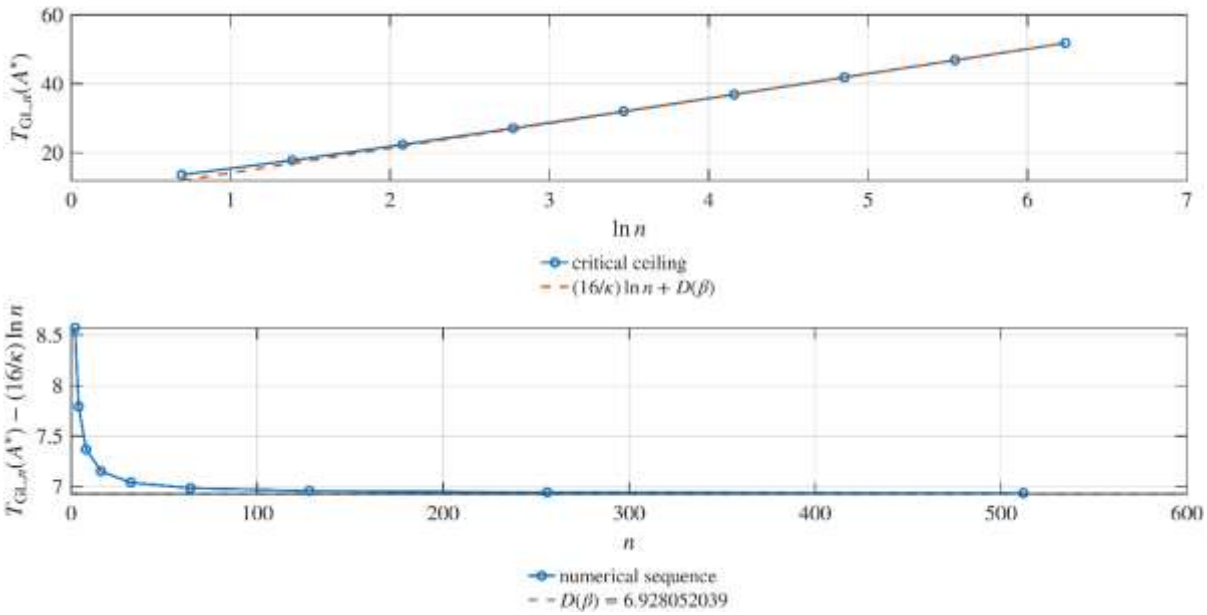


Figure 4. Large-order behavior of the Gauss-Legendre critical ceiling for $\beta = 0.05$. Upper panel: $T_{\mathrm{GL},n}(A^\star)$ compared with the asymptotic law $(16/\kappa)\ln n + D(\beta)$. Lower panel: the residual $T_{\mathrm{GL},n}(A^\star) - (16/\kappa)\ln n$, which converges toward $D(\beta) = 6.928052039048$.

Figures 1–4 and Tables 1–2 numerically illustrate the two limiting regimes analyzed in Sections 3 and 4. Near the critical amplitude, the exact period follows the logarithmic saddle asymptotics, whereas any fixed finite interior-node rule remains bounded. Increasing the Gauss-Legendre order raises this bound only logarithmically. High accuracy at a fixed subcritical amplitude is therefore compatible with the loss of relative accuracy as the critical boundary is approached.

5.4. Cross-family verification of the hard-edge limit

The simultaneous limit in Theorem 4.6 was checked independently of the oscillator by numerical computation. The test uses three parameter-dependent families on $0 \le x \le 2$: family A has $h = 1$, $b = 1$, and $m(\delta) = \delta$; family B has $h = 1 + 0.3x + 0.1\delta$, $b = 1 + 0.2x + 0.15\delta$, and $m(\delta) = \delta + 0.2\delta^2$; family C has $h = 1.4 + 0.25x + 0.1\delta$, $b = 0.6 + 0.4x + 0.05\delta$, and $m(\delta) = 2.3\delta + 0.15\delta^2$. Families A and B share the endpoint triplet $(h_0, b_0, m_1) = (1,1,1)$ despite having different global kernels, while family C has $(1.4,0.6,2.3)$. These choices explicitly test the dependence of the limit on endpoint coefficients rather than on the full integrand.

The recorded computations used quadrature orders $n = 40,80,160,320,640$ at $s = 0.1,1,10$, and also tested endpoint-normalized collapse at $\lambda = 1$. The reference family A has the independently evaluable exact integral $I(\delta) = \operatorname{arsinh}\left(2/\sqrt{\delta}\right)$. At $s = 1$ and $n = 640$, its computed difference $Q_n(0) - Q_n(\delta_n)$ is 0.143718949660, compared with the Bessel-series prediction 0.143718734423; its computed signed error $Q_n(\delta_n) - I(\delta_n)$ is -0.375581777882, compared with the limit -0.375581765740. The calculations use a rationalized difference formula to avoid subtracting nearly equal quadrature sums. The normalized quantities are compared without parameter fitting. The C^1 theorem does not specify a convergence rate.

For a quantitative comparison, the numerical values at $\lambda = 1$ and $n = 640$ are reported as ordered pairs (normalized quadrature difference, normalized signed absolute error): family A, (0.143718949660, -0.375581777882); family B, (0.143718965787, -0.375581550251); and family C, (0.143718075053, -0.375582093029). The common limiting pair is (0.143718734423, -0.375581765740), obtained from the Bessel-series expressions $L(1)$ and $G(1)$. Families A and B use $s = 1$; family C uses $s = 0.2608695652$, as prescribed by $s = b_0/m_1$. The largest absolute difference between a recorded component and its limiting value is 0.000000659370. The comparisons are consistent with the endpoint-normalized limiting profile.

The canonical reference integral has an independently evaluable exact value, so its signed error can be computed without comparing two quadrature implementations. The three kernel families vary their smooth factors while retaining specified endpoint coefficients, allowing the localization in Theorem 4.6 to be tested. Coupling the regularization to quadrature order tests the joint limit rather than fixed-parameter convergence. No parameter fitting enters the limiting profile; these smooth test families do not assess whether the general regularity hypothesis is sharp.

5.5. Error-cancellation profile and finite-order roots

Figure 5 presents the signed limiting function $G(\lambda)$. Its crossings within $(4.15,4.16)$ and $(76.8,77)$ correspond to two certified asymptotic cancellation scales. The approximate limiting values are $\lambda_1 \approx 4.1528672585$ and $\lambda_2 \approx 76.87311692$.

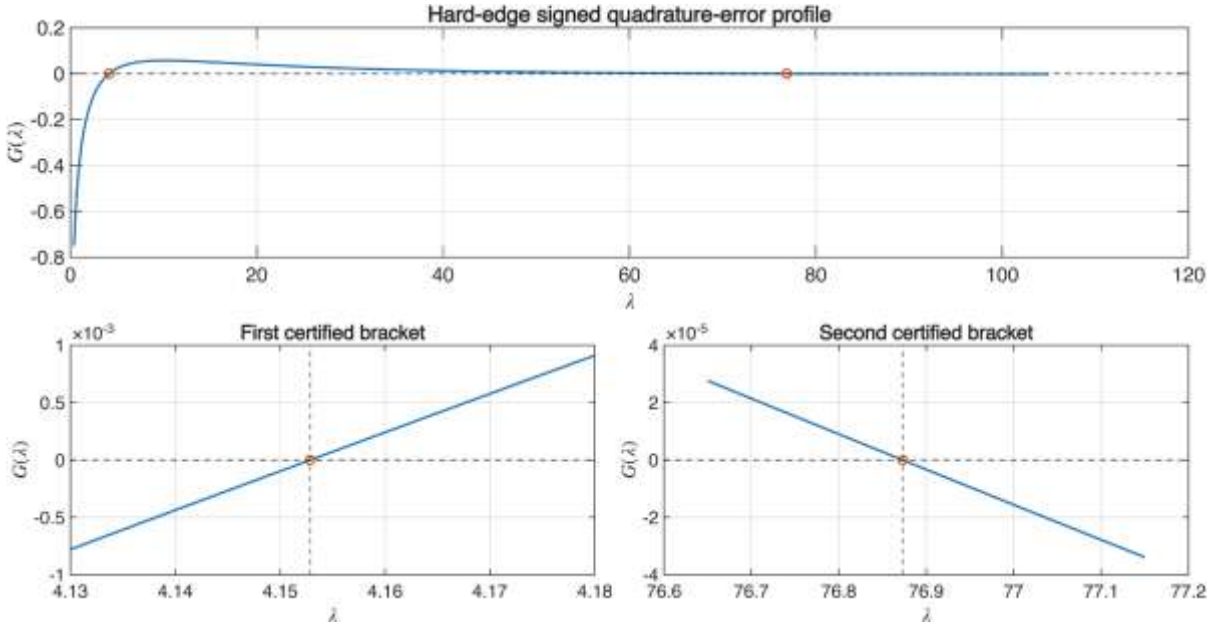


Figure 5. Normalized signed limiting Gauss–Legendre quadrature error $G(\lambda)$ with the two certified zero brackets. The plotted root locations are approximate.

Figure 6 plots the finite-order cancellation behavior for the reference integral and oscillator. The branches recorded in Table 3 approach their respective asymptotic brackets as n increases. At $n = 320$, the first reference and oscillator roots are 4.152902929 and 4.152902930, while the second pair is 76.875792306 and 76.875792444. This decreasing discrepancy supports the normalization in Eq. (4.25).

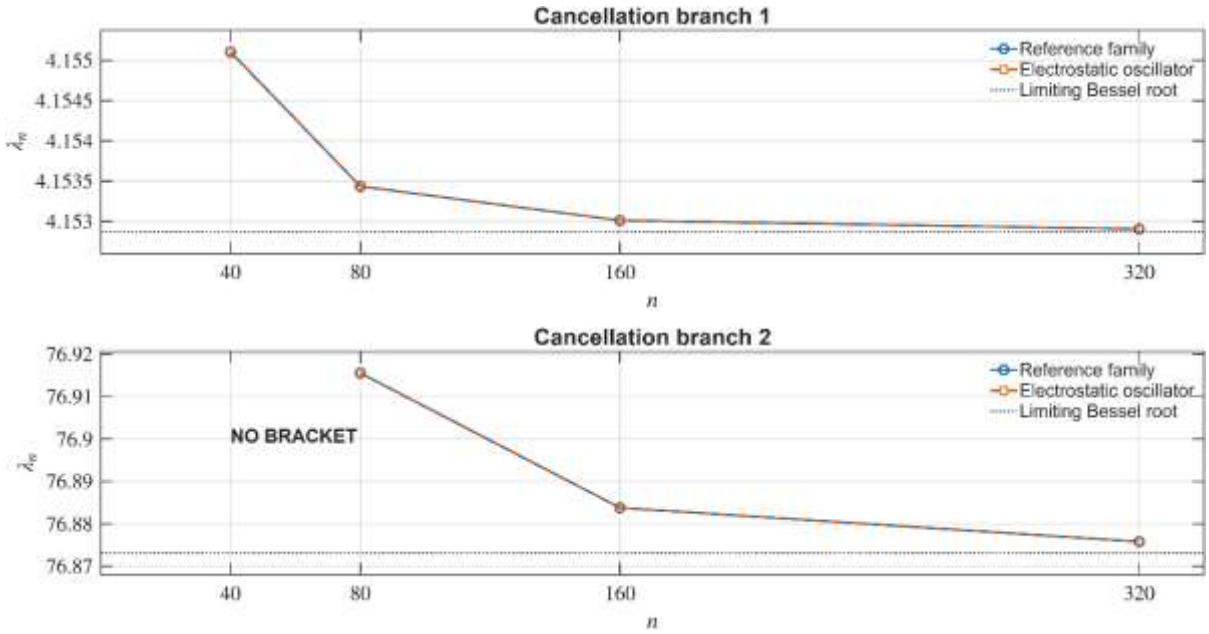


Figure 6. Finite-order signed-error cancellation branches for the reference kernel and the bipolar electrostatic oscillator, independently recomputed by direct numerical evaluation. The curves connect directly calculated finite-order roots for visual comparison; no fitted correction or interpolation was used to determine any root. The second branch at order 40 is labeled NO BRACKET, indicating failure of the specified sign-bracket test only.

Table 3 gives the computed reference and electrostatic-oscillator cancellation parameters at $\beta = 0.05$, as obtained from independent multiprecision recomputation. The first branch is bracketed at $n = 40$, while the second is marked **NO BRACKET** for that order. This means the prescribed numerical bracket did not exhibit the required sign change; it does **not** prove that no second root exists elsewhere. Both branches are recorded at $n = 80,160,320$. The associated oscillator scale s is computed using $s = a\pi^2\lambda/64$ without fitting. The data are consistent with the asymptotic parameter normalization and the *sufficiently-large-order* existence result.

Table 3. Finite-order cancellation parameters for the reference family and electrostatic oscillator at $\beta = 0.05$; all displayed numerical values are rounded from independent multiprecision recomputation.

n	**Branch**	**Reference** λ	**Oscillator** λ	**Oscillator** s
40	1	4.155102982	4.155107174	0.476409791
40	2	NO BRACKET	NO BRACKET	NO BRACKET
80	1	4.153432798	4.153433067	0.476217844
80	2	76.915559046	76.915593725	8.818868054
160	1	4.153009503	4.153009520	0.476169281
160	2	76.883786863	76.883789056	8.815221444
320	1	4.152902929	4.152902930	0.476157060
320	2	76.875792306	76.875792444	8.814304580

5.6. Numerical interpretation and limitations

Figures 1–6 and Tables 1–3 contrast fixed-order critical ceilings with quadrature errors under coupled regularization–order scaling. The computed results for the reference families and oscillator are consistent with the limiting profile. The critical regime cannot be characterized by varying n at a fixed amplitude alone.

6. Conclusions

The analysis establishes a locally uniform double-scaling law for the ordinary, unmodified Gauss–Legendre rule applied to parameter-dependent nearly singular integrals. Under the stated endpoint regularity and positivity hypotheses, the signed absolute quadrature error converges to an explicitly defined Bessel-zero profile when the regularization scale is $\delta = s(n + 1/2)^{-4}$. The leading profile depends on the integral family through its endpoint coefficient and parameter normalization, not through the global shape of the kernel.

For the bipolar electrostatic oscillator, the exact two-term logarithmic critical-period expansion and the finite-order quadrature ceiling provide a physical baseline. The coupled-order analysis sharpens this picture: for $a - A = sN^{-p}$ with fixed $s > 0$, the absolute quadrature error tends to zero when $0 < p < 4$, has a finite generally nonzero limit at $p = 4$, and develops the limiting relative-error ratio $4/p - 1$ for $p > 4$. The first assertion relies on oscillator-specific analyticity, which is not assumed in the general C^1 theorem.

Analytical tail estimates combined with finite-sum interval enclosures establish a simple limiting zero in each of two disjoint intervals of the normalized error profile. Local uniform convergence and continuity also yield finite-order exact-error cancellation parameters in each interval for all sufficiently large quadrature orders. The existence statement is restricted to these intervals and sufficiently large orders.

The analysis complements fixed-integrand endpoint expansions, including those of Sidi[2], by treating the coupled parameter–order limit directly. The cancellation scales identify isolated zero-error parameters rather than uniformly small errors in their neighborhoods.

Convergence at a *fixed* subcritical parameter does not determine the error when the parameter simultaneously approaches its singular limit. The critical N^{-4} scale and signed-error profile characterize this coupled regime.

Under stronger but only frozen C^3 coefficient regularity, we have also obtained a locally uniform next-order correction to the signed error. Its canonical part is complemented by two spatial endpoint-slope terms. A constructive joint C^1 example demonstrates that the corresponding global approximation assumption cannot be omitted merely by retaining the same endpoint slopes; the stronger sufficient condition is not claimed to be sharp.

The correction governs the N^{-2} displacement of any selected exact finite-order cancellation root from either certified simple limiting zero, without implying finite-order root uniqueness. In the bipolar oscillator, vanishing endpoint slopes simplify this result and give an $o(N^{-6})$ remainder for the corrected cancellation amplitude. The underlying Legendre-ratio representation and special-

function endpoint expansions are established analytical tools; the result is their parameter-dependent signed-error consequence under the specified double scaling.

The results are restricted to the stated parameter-dependent kernel class and, for the detailed physical interpretation, an undamped, unforced single-degree-of-freedom conservative oscillator. General C^1 data do not imply the oscillator's analytic $p < 4$ error bound. Adaptive, singularity-subtracted, or parameter-dependent-node quadrature schemes are not evaluated here.

Appendix A. Analytical tail controls and sign-certification details

The fixed-index Bessel endpoint limit in Theorem 4.6 must be combined with a summable estimate before one may pass to an infinite quadrature sum. For shifted Gauss–Legendre nodes numbered from the left, classical Legendre zero-angle inequalities give $x_{k,n} \geq C_1 k^2 N^{-2}$. The Chebyshev–Markov–Stieltjes inequalities imply $w_{k,n} \leq C_2 k N^{-2}$ for the first half of the nodes, with constants independent of n and k. The remaining nodes have $x_{k,n} \geq C_3 > 0$. Hence the bound $|f_0(x) - f_\delta(x)| \leq C\delta x^{-3}$ yields the uniform remainder $\sum_{k>K} w_{k,n} \left|f_0(x_{k,n}) - f_{sN^{-4}}(x_{k,n})\right| \leq CsK^{-4} + CsN^{-4}$. This summability argument is essential: fixed-index asymptotics alone do not justify interchanging a limit and a growing sum.

More explicitly, the cumulative Gauss weights bracket the ordered shifted nodes by the classical Chebyshev–Markov–Stieltjes inequalities. Subtracting two consecutive cumulative-weight bounds controls each interior weight by the gap between its neighboring nodes; the first weight is handled by the one-sided endpoint inequality. Together with the standard Legendre zero-spacing bounds, this yields the weight estimate invoked above. The uniform tail is summable because its terms decay at least at the fifth power of the node index.

To specify the weight inequality, write $W_{k,n} = \sum_{j=1}^{k} w_{j,n}$. For the uniform measure on $[0,2]$, the Chebyshev–Markov–Stieltjes bounds, with the nodes ordered from the left, read

$$W_{k-1,n} \leq x_{k,n} \leq W_{k,n} \leq x_{k+1,n}, \qquad 1 \leq k < n.$$

Thus, for $2 \leq k < n$, $w_{k,n} = W_{k,n} - W_{k-1,n} \leq x_{k+1,n} - x_{k-1,n}$; also $w_{1,n} \leq W_{2,n} \leq x_{3,n}$ when $n \geq 3$. These formulae, together with the Legendre zero-angle spacing estimate, supply $w_{k,n} \leq CkN^{-2}$ on the first half of the nodes. Substituting $x_{k,n} \geq Ck^2N^{-2}$ and $\delta = sN^{-4}$ gives $w_{k,n}\delta x_{k,n}^{-3} \leq Csk^{-5}$. Summation yields CsK^{-4}, while the remaining nodes contribute $O(sN^{-4})$ because their abscissas are bounded away from zero.

The existence of cancellation scales requires a sign determination for the complete infinite series, not just roots of a truncated graph. This appendix records the inequalities used in Section 4.5. Write j_k for the kth positive zero of J_0, $v_k = j_k^2/2$ and

$$L_K(\lambda) = 2\sum_{k=1}^{K} \frac{1}{J_1(j_k)^2}\left(\frac{1}{v_k} - \frac{1}{\sqrt{v_k^2 + \lambda}}\right).$$

At the zeros of J_0, the Bessel Wronskian and Nicholson's integral bound give $J_1(j_k)^{-2} < \pi j_k/2$. Combining this inequality with $j_k \geq \pi(k - 1/4)$ and

$$0 < \frac{1}{v} - \frac{1}{\sqrt{v^2+\lambda}} \le \frac{\lambda}{2v^3}$$

shows that the kth term of L is no larger than $4\lambda/[\pi^4(k-1/4)^5]$. The integral comparison for this decreasing sequence yields the bound cited in Section 4.5:

$$0 < L(\lambda) - L_K(\lambda) < \frac{\lambda}{\pi^4(K-1/4)^4}.$$

Termwise differentiation of the absolutely convergent Bessel series gives

$$G'(\lambda) = \frac{1}{2\lambda} - \sum_{k=1}^{\infty} \frac{1}{J_1(j_k)^2(v_k^2+\lambda)^{3/2}}.$$

If $S_K(\lambda)$ is the truncated derivative sum and $\varepsilon_K = [\pi^4(K-1/4)^4]^{-1}$, its strictly decreasing terms imply $0 < S(\lambda) - S_K(\lambda) < \varepsilon_K$. Thus for $0 < a \le \lambda \le b$,

$$\frac{1}{2b} - S_K(a) - \varepsilon_K < G'(\lambda) < \frac{1}{2a} - S_K(b).$$

For $K = 24$, the tail constant is $\varepsilon_{24} \approx 3.2266068642 \times 10^{-8}$. The numerical certification brackets each Bessel zero by opposite signs of the defining Bessel function, encloses the associated Bessel values by interval evaluation, and combines the resulting finite-sum interval with the explicit analytical tail bounds. Interval enclosures of $j_1, \dots, j_{24}$, $J_1(j_k)$, and the finite sums, combined with the analytical remainder bounds, yield the four strict signs reported in Section 4.5. The corresponding certified derivative ranges are $0.03362924 < G'(\lambda) < 0.03401947$ throughout $(4.15,4.16)$ and $-0.000140681 < G'(\lambda) < -0.000105559$ throughout $(76.8,77)$. These computations distinguish interval-certified signs from the approximate decimal roots plotted in Figure 5. The enclosures were independently reproduced by an interval-arithmetic computation with outward rounding for the finite series and its analytic remainder. The certificate verifies the indexed Bessel-zero brackets, all four signed endpoint enclosures, and the derivative signs throughout both specified brackets.

The reproducible enclosure procedure evaluates 24 indexed Bessel zeros using 100-decimal-digit seed approximations, 110-decimal-digit outward-rounded interval arithmetic, and 281 terms of the defining Taylor series for each Bessel-function evaluation. Rational endpoint brackets are formed within 1e-26 of each high-precision seed; opposite interval-certified Bessel signs and disjoint classical zero-index bounds validate their indexing independently of the seeds. Taylor remainders are enclosed by an interval-evaluated geometric majorant, and neighboring Bessel values are extended from the decimal seed to the whole root bracket using a derivative bound of one in absolute value. For each index from 1 through 24, locate the J_0 zero between consecutive rational endpoints with opposite interval-certified Bessel signs, evaluate J_1 on that enclosing interval, and form interval bounds for the 24 corresponding summands. For each of $\lambda = 4.15,4.16,76.8,77$, evaluate $2\gamma - \log 4 + (\log\lambda)/2 - L_{24}(\lambda)$ with outward rounding; enlarge the interval by $\lambda\varepsilon_{24}$ on the lower side to account for the strictly positive omitted tail. For derivatives on either closed root bracket $[a,b]$, use the endpoint monotonicity of the truncated derivative sum and the explicit bounds

$$\frac{1}{2b} - S_{24}(a) - \varepsilon_{24} < G'(\lambda) < \frac{1}{2a} - S_{24}(b), \qquad a \le \lambda \le b.$$

The enclosed signs and derivative bounds displayed in the main text are the outputs to be independently reproduced. This finite calculation certifies only the existence and uniqueness of one root within each stated bracket; it gives no information about possible roots elsewhere.

Appendix B. Numerical provenance and interpretation

Figures 1–4 and Tables 1–2 use archived oscillator computations; the estimates in Table 1 are obtained by three-distance Richardson extrapolation. The three-kernel comparisons are independent calculations, and Table 3 reports independently recomputed numerical cancellation parameters for $\beta = 0.05$. The transformation from a normalized limiting parameter to the oscillator parameter is $s = a\pi^2\lambda/64$. Figure 5 was generated from 2000 Bessel zeros; the interval sign certificates follow the separate procedure in Appendix A. Figure 6 was independently recomputed by solving the signed-error equations for the reference and electrostatic integrals, rather than interpolating Table 3. The plotted finite-order roots agree with multiprecision recomputations to the resolution of the graph. The tabulated values are numerical approximations, not interval-certified root enclosures.

Independent checks conducted on 6 November 2026 used 55-digit working precision for the eight Table 1 closed-form constants and all ten rows of Table 2; all differences lie within the reported decimal rounding. Table 3 roots were reevaluated using 47-digit working precision, high-precision Legendre nodes and weights, and separate quadrature of the exact oscillator period. The root calculations, analytic coefficients, and rounding are archived with the numerical recheck scripts; the values are numerical approximations, not interval-certified root enclosures.

The entry NO BRACKET for the second branch at $n = 40$ denotes failure of the prescribed sign-bracketing test; it does not establish nonexistence of a root. Both branches were computed for $n = 80,160,320$. Proposition 4.8 gives the asymptotic existence statement for sufficiently large quadrature orders.

Appendix C. Uniform complex remainder and Legendre counterexample details

The following technical arguments supplement Lemma 4.9 and Example 4.11. They distinguish the vanishing auxiliary Wronskian remainder from the generally nonvanishing remainder of the Legendre ratio itself.

C.1. Locally uniform remainder for the Legendre ratio

Set $N = n + 1/2,\ \varepsilon = N^{-2}$, and

$$p_n(\zeta) \quad = P_n(1+\varepsilon\zeta), \quad p_0(\zeta) \quad = I_0\left(\sqrt{2\zeta}\right),\ r_n(\zeta) \quad = \mathrm{Q}_n(1+\varepsilon\zeta)/p_n(\zeta), \quad r_0(\zeta) \quad = K_0\left(\sqrt{2\zeta}\right)/p_0(\zeta).$$

The exact finite Legendre series is

$$p_n(\zeta) = \sum_{k=0}^{n} \frac{(\zeta/2)^k}{(k!)^2} \prod_{j=0}^{k-1} [1 - \varepsilon(j+1/2)^2].$$

The factorial denominator, together with splitting the index at a fixed large cutoff before expanding the products, yields uniformly on every fixed complex compact set

For completeness, put $a_j = \varepsilon(j+1/2)^2$ and $S_k = \sum_{j=0}^{k-1}(j+1/2)^2 = k(4k^2-1)/12$. For $k \le n$ one has $0 \le a_j < 1$. Apply Taylor's theorem to $F_k(u) = \prod_{j=0}^{k-1}(1-ua_j)$ on $0 \le u \le 1$: since $0 \le F_k''(u) \le \left(\sum_{j<k} a_j\right)^2$, it follows that

$$0 \le \prod_{j=0}^{k-1}(1-a_j) - (1-\varepsilon S_k) \le 1/2\,\varepsilon^2 S_k^2 \le C\varepsilon^2 k^6.$$

On each compact set $|\zeta| \le R$, the series $\sum_{k\ge 0}(R/2)^k\, k^6/(k!)^2$ converges. Its product-remainder contribution is therefore $O_R(\varepsilon^2)$; the omitted $k > n$ terms in the full Bessel series and its first correction are $o_R(\varepsilon^2)$ by factorial decay. This proves $p_n = p_0 + \varepsilon p_1 + O_R(\varepsilon^2)$ uniformly on complex compacta, with $p_1 = -(4D^3 - D)p_0/12$ and $D = \zeta\,\partial_\zeta$. Cauchy's estimates on a slightly larger compact set justify the derivative bounds used below.

$$p_n = p_0 + \varepsilon p_1 + O(\varepsilon^2), \qquad p_1 = -\frac{\zeta}{6}p_0 - \frac{\zeta(2\zeta-1)}{12}p_0'.$$

The zeros of p_0 lie on the strictly negative real axis. For each compact $J \subset (0,\infty)$, choose nested bounded simply connected neighborhoods $V \Subset U$ of the imaginary segments $i\left[-\sqrt{\max J}, \sqrt{\max J}\right]$, with $\overline{U}$ disjoint from the zeros of p_0. Since $p_n \to p_0$ uniformly on $\overline{U}$, p_n is nonzero there for large n.

Define

$$T_n(\zeta) = [(1+\varepsilon\zeta/2)p_n(\zeta)^2]^{-1},\ T_0(\zeta) = p_0(\zeta)^{-2},\ T_1(\zeta) = -\frac{\zeta}{2p_0(\zeta)^2} - \frac{2p_1(\zeta)}{p_0(\zeta)^3},\ D_n(\zeta) = T_n(\zeta) - T_0(\zeta$$

Then D_n is holomorphic on U, $\sup_U |D_n| = O(\varepsilon^2)$, and, crucially,

$$D_n(0) = 0.$$

Cauchy's estimate on a fixed disk around zero and the direct sup-norm bound away from that disk imply

$$\sup_{\zeta\in V}|D_n(\zeta)/\zeta| = O(\varepsilon^2),$$

where the quotient is extended analytically at zero. By the Legendre Wronskian,

$$r_n' = -T_n/(2\zeta), \qquad r_0' = -T_0/(2\zeta), \qquad r_1' = -T_1/(2\zeta),$$

with

$$r_1(\zeta) = \frac{2\zeta-1}{24p_0(\zeta)^2}.$$

Consequently, the derivative of $F_n = r_n - r_0 - \varepsilon r_1$ is holomorphic across zero and satisfies $\sup_V |F_n'| = O(\varepsilon^2)$. The exact constant from the logarithmically regularized ratio is

$$F_n(0) = \log N + \gamma - H_n + \frac{\varepsilon}{24} = \frac{7}{960}\varepsilon^2 + O(\varepsilon^3).$$

Integrating F_n' along bounded fixed paths in V proves

$$r_n(\zeta) = r_0(\zeta) + \varepsilon r_1(\zeta) + O_V(\varepsilon^2).$$

This bound is locally uniform through $\zeta = 0$ and justifies termwise integration of the Cauchy representation on the moving imaginary segment. In particular, it is $D_n(0)$, **not** $F_n(0)$, that vanishes exactly; no quotient $F_n(\zeta)/\zeta$ is used.

C.2. Exact moment and lacunary-tail analysis

For $m \geq 2$ let $\Phi_m(t) = (1-t^2)^2 P_m(t)^2$. The three-term Legendre recurrence gives

$$tP_m(t) = \frac{m+1}{2m+1} P_{m+1}(t) + \frac{m}{2m+1} P_{m-1}(t).$$

Applying it a second time yields

$$t^2 P_m = A_m P_{m+2} + B_m P_m + C_m P_{m-2},$$

where

$$A_m = \frac{(m+1)(m+2)}{(2m+1)(2m+3)},\ B_m = \frac{(m+1)^2}{(2m+1)(2m+3)} + \frac{m^2}{(2m+1)(2m-1)},\ C_m = \frac{m(m-1)}{(2m+1)(2m-1)}.$$

Orthogonality and $\int_{-1}^{1} P_k(t)^2 dt = 2/(2k+1)$ give

$$\int_{-1}^{1} \Phi_m(t) dt = \| P_m \|_2^2 - 2\langle P_m, t^2 P_m \rangle + \| t^2 P_m \|_2^2 = \frac{4(3m^4 + 6m^3 - 11m^2 - 14m + 12)}{(2m-3)(2m-1)(2m+1)(2m+3)(2m+5)} = \frac{7}{8}$$

The standard bounds for Legendre polynomials on the interval, together with the factor $(1-t^2)^2$, yield $\| \Phi_m \|_\infty = O(m^{-1})$ and $\| \Phi_m' \|_\infty = O(1)$. Therefore the series defining g and g' in Example 4.11 converge uniformly. Because each $\Phi_m(t)$ contains the endpoint factor $(1-t^2)^2$, the conditions $g(0) = g'(0) = 0$ follow.

Here the required weighted bounds follow from an explicit classical inequality, rather than being assumptions on the example. The Bernstein–Jacobi inequality (NIST Digital Library of Mathematical Functions, Eq. 18.14.3, specialized to Legendre polynomials) gives, for every $m \geq 1$ and $-1 < t < 1$,

$$|P_m(t)| \leq \sqrt{\frac{2}{\pi(m+1/2)}} (1-t^2)^{-1/4}.$$

Set $v = 1 - t^2$. The preceding inequality implies $|\Phi_m(t)| = v^2 P_m(t)^2 \leq 2v^{3/2}/[\pi(m + 1/2)] \leq C/m$. Further, the exact Legendre recurrence $vP_m'(t) = m[P_{m-1}(t) - tP_m(t)]$ yields

$$|\Phi_m'(t)| \leq 4vP_m(t)^2 + 2mv|P_m(t)|(|P_{m-1}(t)| + |P_m(t)|) \leq C\left(m^{-1}v^{1/2} + v^{1/2}\right) \leq C.$$

The endpoints are covered by continuity, because the factor v^2 makes both Φ_m and $\Phi_m{}'$ vanish there. The estimates are uniform in $m \geq 2$, and $\sum_j a_j < \infty$, so the series defining g and g' converge uniformly on $[0,2]$. The same endpoint factor gives $g(0) = g'(0) = 0$; moreover $|P_m(t)| \leq 1$ on $[-1,1]$ implies $g(x) \leq Cx^2$. Together with the exact moment and the lacunary-tail estimate below, this proves the counterexample under the stated joint C^1 regularity.

For $n = m_j = 2^{2^j}$, the earlier terms Φ_{m_i}, $i < j$, have degree $2m_i + 4 \leq 2n - 1$ and are therefore integrated exactly by Q_n. The j-th term has a factor $P_n(x-1)^2$ and vanishes at every quadrature node; its quadrature error is minus the moment above. For the later terms, positivity and the supremum bound give

$$\left| \sum_{i>j} a_i \, \mathcal{E}_{m_j}[\Phi_{m_i}(\cdot - 1)] \right| \leq 4C \sum_{i>j} \frac{a_i}{m_i} = o\big(a_j/m_j\big).$$

Thus $\mathcal{E}_{m_j}[g] \sim -3a_j/\big(8m_j\big)$, and $N^2 \mathcal{E}_{m_j}[g] \to -\infty$. Finally, $0 \leq g(x) \leq Cx^2$ implies $g(x)\big(1 - q_{\lambda N^{-4}}(x)\big) \leq C_J N^{-4}$, so its quadrature error is also $O_J(N^{-4})$. This establishes the claimed failure of a universal N^{-2} correction under joint C^1 alone.

Acknowledgments

This research is supported by the Research Support Scheme of the National Science and Technology Council, Taiwan [grant no. NSTC114-2222-E-992-006].

Conflict of interest

The authors declare no conflicts of interest.

References

1. D. S. Lubinsky, P. Rabinowitz, Rates of convergence of Gaussian quadrature for singular integrands, *Math. Comp.*, **43** (1984), 219–242. https://doi.org/10.1090/S0025-5718-1984-0744932-2.
2. A. Sidi, Asymptotic expansions of Gauss-Legendre quadrature rules for integrals with endpoint singularities, *Math. Comp.*, **78** (2009), 241–253. https://doi.org/10.1090/S0025-5718-08-02135-2.
3. D. Huybrechs, R. Cools, On Generalized Gaussian Quadrature Rules for Singular and Nearly Singular Integrals, *SIAM J. Numer. Anal.*, **47** (2009), 719–739. https://doi.org/10.1137/080723417.
4. W. Van Assche, I. Vanherwegen, Quadrature formulas based on rational interpolation, *Math. Comp.*, **61** (1993), 765–783. https://doi.org/10.1090/S0025-5718-1993-1195424-6.
5. F. W. Olver, D. W. Lozier, R. Boisvert, C. W. Clark, The NIST Handbook of Mathematical Functions, Cambridge University Press, New York, NY, 2010.

6. P. J. Davis, P. Rabinowitz, Methods of Numerical Integration, Academic Press, 1984. https://doi.org/10.1016/C2013-0-10566-1.
7. D. Elliott, B. M. Johnston, P. R. Johnston, Clenshaw–Curtis and Gauss–Legendre Quadrature for Certain Boundary Element Integrals, *SIAM J. Sci. Comput.*, **31** (2008), 510–530. https://doi.org/10.1137/07070200X.
8. W. Mitchell, A. Natkin, P. Robertson, M. Sullivan, X. Yu, C. Zhu, Decomposition and conformal mapping techniques for the quadrature of nearly singular integrals, *Bit Numer Math*, **63** (2023), 41. https://doi.org/10.1007/s10543-023-00984-w.
9. E. M. Abdel-Rahman, M. I. Younis, A. H. Nayfeh, Characterization of the mechanical behavior of an electrically actuated microbeam, *J. Micromech. Microeng.*, **12** (2002), 759–766. https://doi.org/10.1088/0960-1317/12/6/306.
10. Y. Fu, J. Zhang, L. Wan, Application of the energy balance method to a nonlinear oscillator arising in the microelectromechanical system (MEMS), *Current Applied Physics*, **11** (2011), 482–485. https://doi.org/10.1016/j.cap.2010.08.037.
11. Y. Khan, M. Akbarzade, Dynamic Analysis of Nonlinear Oscillator Equation Arising in Double-Sided Driven Clamped Microbeam-Based Electromechanical Resonator, *Zeitschrift für Naturforschung A*, **67** (2012), 435–440. https://doi.org/10.5560/zna.2012-0043.
12. Y. H. Qian, D. X. Ren, S. K. Lai, S. M. Chen, Analytical approximations to nonlinear vibration of an electrostatically actuated microbeam, *Communications in Nonlinear Science and Numerical Simulation*, **17** (2012), 1947–1955. https://doi.org/10.1016/j.cnsns.2011.09.018.
13. S. Sadeghzadeh, A. Kabiri, Application of Higher Order Hamiltonian Approach to the Nonlinear Vibration of Micro Electro Mechanical Systems, *Lat. Am. j. solids struct.*, **13** (2016), 478–497. https://doi.org/10.1590/1679-78252557.
14. S. K. Lai, X. Yang, C. Wang, W. J. Liu, An Analytical Study for Nonlinear Free and Forced Vibration of Electrostatically Actuated MEMS Resonators, *Int. J. Str. Stab. Dyn.*, **19** (2019), 1950072. https://doi.org/10.1142/S021945541950072X.
15. H. Mobki, G. Rezazadeh, M. Sadeghi, F. Vakili-Tahami, M.-M. Seyyed-Fakhrabadi, A comprehensive study of stability in an electro-statically actuated micro-beam, *International Journal of Non-Linear Mechanics*, **48** (2013), 78–85. https://doi.org/10.1016/j.ijnonlinmec.2012.08.002.
16. M. M. Joglekar, D. N. Pawaskar, Estimation of oscillation period/switching time for electrostatically actuated microbeam type switches, *International Journal of Mechanical Sciences*, **53** (2011), 116–125. https://doi.org/10.1016/j.ijmecsci.2010.12.001.
17. A. Gutiérrez, P. J. Torres, NONAUTONOMOUS SADDLE-NODE BIFURCATION IN A CANONICAL ELECTROSTATIC MEMS, *Int. J. Bifurcation Chaos*, **23** (2013), 1350088. https://doi.org/10.1142/S0218127413500880.
18. Z. Cheng, C. Kong, Q. Yuan, Nonlinear dynamics of periodic solutions in electrostatic MEMS: Theory and numerical bifurcation analysis, *Physica D: Nonlinear Phenomena*, **482** (2025), 134887. https://doi.org/10.1016/j.physd.2025.134887.
19. L. D. Landau, E. M. Lifshitz, Mechanics, Pergamon, Oxford, 1994.
20. M. Saavedra, Asymptotic expansion of the period function, *Journal of Differential Equations*, **193** (2003), 359–373. https://doi.org/10.1016/S0022-0396(03)00091-3.

21. B. Wu, W. Liu, C. W. Lim, H. Zhong, Explicit approximate frequency–amplitude relationships for conservative nonlinear oscillators, *Applied Mathematical Modelling*, **157** (2026), 116851. https://doi.org/10.1016/j.apm.2026.116851.
22. T. Zhu, L. Qin, S.-K. Lai, H. Zhong, B. Wu, Explicit High-Accuracy Approximations for the Period of Large-Amplitude String Vibrations, *Int. J. Str. Stab. Dyn.*, **27** (2027), 2771006. https://doi.org/10.1142/S0219455427710064.
23. The MathWorks Inc., MATLAB (R2026b), (2026).